



Article

Evaluation and Projection of Precipitation in CMIP6 Models over the Qilian Mountains, China

Xiaohong Yang^{1,2}, Weijun Sun¹, Jiake Wu¹, Jiahang Che¹, Mengyuan Liu¹, Qinglin Zhang¹, Yingshan Wang¹, Baojuan Huai¹, Yuzhe Wang¹ and Lei Wang^{1,*}

¹ College of Geography and Environment, Shandong Normal University, Jinan 250014, China

² The First Middle School of Yucheng City, Dezhou 251200, China

* Correspondence: sdwanglei@lzb.ac.cn

Abstract: The Qilian Mountains (QMs) act as the “water tower” of the Hexi Corridors, playing an important role in the regional ecosystem security and economic development. Therefore, it is of great significance to understand the spatiotemporal characteristics of precipitation in the QMs. This study evaluated the performance of 21 models of phase 6 of the Coupled Model Intercomparison Project (CMIP6) from 1959 to 1988 based on ERA5 and in situ datasets. In addition, the precipitation changing trend from 2015 to 2100 was projected according to four shared socioeconomic pathways (SSPs): namely, SSP126, SSP245, SSP370, and SSP585. The results have shown the following: (1) all CMIP6 models could reflect the same precipitation changing trend, based on the observed datasets ($-2.01 \text{ mm}\cdot 10\text{a}^{-1}$), which was slightly lower than that of ERA5 ($2.82 \text{ mm}\cdot 10\text{a}^{-1}$). Multi-mode ensemble averaging (MME) showed that the projected precipitation-change trend of the four scenarios was 5.73, 9.15, 12.23, and 16.14 $\text{mm}\cdot 10\text{a}^{-1}$, respectively. (2) The MME and ERA5 showed the same precipitation spatial pattern. Also, during the period 1959–1988, the MME in spring, summer, autumn and winter was 130.07, 224.62, 95.96, and 29.07 mm, respectively, and that of ERA5 was 98.57, 280.77, 96.85, and 22.64 mm, respectively. The largest precipitation difference in summer was because of strong convection and variable circulation. (3) From 2015 to 2100, the snow-to-rain ratio was between 0.1 and 1.1, and the snow-to-rain ratio climate tendency rate was concentrated in the range of $-10\sim-0.1 \text{ mm}\cdot 10\text{a}^{-1}$. Both of these passed the significance test ($p < 0.05$). The projected rainfall of all four SSPs all showed an increasing trend with values of 6.20, 11.31, 5.64, and 20.41 $\text{mm}\cdot 10\text{a}^{-1}$, respectively. The snowfall of the four SSPs all showed a decreasing trend with values of 0.42, 2.18, 3.34, and 4.17 $\text{mm}\cdot 10\text{a}^{-1}$, respectively.

Keywords: Qilian Mountains; CMIP6; precipitation; global climate model



Citation: Yang, X.; Sun, W.; Wu, J.; Che, J.; Liu, M.; Zhang, Q.; Wang, Y.; Huai, B.; Wang, Y.; Wang, L. Evaluation and Projection of Precipitation in CMIP6 Models over the Qilian Mountains, China. *Remote Sens.* **2023**, *15*, 4350. <https://doi.org/10.3390/rs15174350>

Academic Editor: Hatim Sharif

Received: 4 August 2023

Revised: 17 August 2023

Accepted: 1 September 2023

Published: 4 September 2023



Copyright: © 2023 by the authors. Licensee MDPI, Basel, Switzerland. This article is an open access article distributed under the terms and conditions of the Creative Commons Attribution (CC BY) license (<https://creativecommons.org/licenses/by/4.0/>).

1. Introduction

Precipitation plays an important role in the social and economic development of northwest China. The QMs are representative arid and semi-arid areas that are affected by a westerly wind belt, southern monsoons (the south Asian monsoon and the plateau monsoon) and east Asian monsoons [1]. River runoff in the alpine region mainly comes from local precipitation and glacier melting in the warm season [2,3]. In recent decades, the occurrence of precipitation and flood events in the desert in northwest China has posed a problem to the area’s human population. Over the past half-century, the climate appears to have been the wettest it has been in 3500 years [4]. It is urgently necessary to further evaluate the regional precipitation status to provide a scientific basis for designing industrial and agricultural layout and related policies.

Rapid warming trends in the mid-latitudes of the northern hemisphere have previously confirmed that this could result in accelerated regional and global water cycles [5]. Rising temperatures will ultimately result in rising sea levels, losses in terms of glacier area, coast-line retreat, etc., along with increasing the occurrence of high-temperature droughts, heavy

rainfall and flood events [6]. From 1951 to 2012, the global average surface temperature increased at a rate of $0.12\text{ }^{\circ}\text{C}\cdot 10\text{a}^{-1}$, which is almost double the rate for 1880 to 1898 [7]. The QMs are a highly climate-sensitive area in the northwest of China. Extreme precipitation events have significant effects on this ecological environment. In recent decades, precipitation in the QMs has shown a significant increase and the results of ERA5-Land showed that the average climate tendency rate of precipitation in the QMs reached $15.43\text{ mm}\cdot 10\text{a}^{-1}$ in the period from 1980 to 2018 [8]. Shi et al. (2002) had reported that the climate of the QMs and the surrounding areas indicated a warming phenomenon [9]. This phenomenon was also reported to show that the arid and semi-arid northwest region experienced a sharp increase in precipitation after the mid-1980s [10,11]. However, it remains unclear as to how extreme precipitation events will affect surface and groundwater resources, agricultural production, and economic growth in the context of global warming in the QMs. Thus, it is important to identify the long-term changes in precipitation and the physical mechanisms associated with precipitation in the region. Additionally, it is highly important to predict future precipitation and its phase change in the QMs. This study aimed to evaluate the precipitation situation and predict future precipitation changes in the QMs.

The QMs are a region of synergistic influence of multiple complex climate systems. They are the water source of the Shule River, the Shi Yang River, the Black River, the Qinghai Lake system and the Datong River, which is an important tributary of the Yellow River. They also provide an important ecological barrier in the arid and semi-arid regions of northwest China. Therefore, it is of great significance to understand the proportion of solid-liquid precipitation in the QMs and associated temporal and spatial changes. This study is conducive to constructing a reasonable ecological barrier based on water resources and their related changes in the QMs [1,12].

The difficulty of obtaining accurate historical precipitation datasets in the QMs mainly relates to the complex topography and precipitation process in this region, the significant altitude differences, and the existence of few long-term precipitation automatic weather stations (AWSs) [13]. The lack of high-quality, high-resolution, long-term continuous global observational data, the limitations of rough spatial resolution, and model uncertainties are the biggest obstacles. They affect the in-depth understanding and understanding of the causes and evolution of climate change, and they are also the biggest stumbling blocks in the progress of atmospheric science research [14].

GCMs currently represent the main methods of assessing historical climate characteristics and projecting future climate change in recent years. The Coupled Model InterComparison Project (CMIP) has been widely used in climate change assessments and projections [15–18]. Li et al. [19] used CMIP5 data to examine the temperature and precipitation of the Qinghai–Tibet Plateau and concluded that the average performance of 44 patterns was generally better than that of most single patterns. The equal-weight-set average scheme proved to be better than the median average. The ensemble average of the selected models could improve the overall simulation ability, and the improvement in the precipitation simulation was more significant. Wu et al. [20] assessed the temperature and precipitation in the arid and semi-arid northwest region of China. By comparing the ensemble average of 15 groups of CMIP3 and CMIP5 models to simulate the temperature and precipitation in this region, it was found that the CMIP5 model was closer to the observed temperature and precipitation. Some studies have shown that the spatial correlation coefficient between the global average annual precipitation simulated by the CMIP5 model and the measured values was as high as 0.8 [21]. However, other studies have shown that the CMIP5 data had a significant wet deviation and exhibited greater uncertainty in the precipitation data [22].

Although the above studies have comprehensively investigated precipitation events in the QMs, a major part of this research is limited to studying future changes in precipitation in the warming scenario, or else it uses GCMs from CMIP5 and regional climate models (RCMs). This study used CMIP6 to estimate precipitation and the snow-to-rain ratio in

the QMs, which is important for quantifying socioeconomic risks for policymakers and developing climate adaptation strategies with risk reduction measures.

GCMs have different initial conditions, parameterizations, spatial and temporal resolutions, and boundary conditions, which affect the output of the model. It is necessary to evaluate the model output prior to use in different applications [23,24]. Compared with CMIP5, CMIP6 had effectively designed science experiments, more models, more data, and higher resolutions [25,26], and its simulation effect for climate change prediction improved significantly compared with the previous stages [27,28]. Therefore, in terms of future experimental designs, the CMIP6 model was used to predict the precipitation and snowfall ratio under different scenarios in the QMs.

Additionally, CMIP6 has upgraded its new future scenarios, with the combination of radiative forcing levels of the representative concentration pathways used in the 5th phase of CMIP and the shared socioeconomic pathways (SSPs) [29–31], which makes them more reasonable. Scenario MIP is one of the core MIP experiments in CMIP6. Considering future CO₂, CH₄, N₂O, and other gas concentrations, as well as land use, the design of Scenario MIP involves eight pathways, including two tiers (tier 1 and tier 2) of priority. Tier-1 includes four combined SSPs with radiative forcing, i.e., SSP126, SSP245, SSP370, and SSP585, in which the globally averaged radiative forcing at the top of the atmosphere around the year 2100 is predicted to be approximately 2.6, 4.5, 7.0, and 8.5 W m⁻², respectively [29,32]. Since this study period ends in 2100, we used tier 1. In addition to using a long research time series (1959–2100), this study also involved rainfall and snowfall as well as the ratio of snow to rain. Some model data were missing and put forward some abnormal performance models. This study finally selected 21 models of CMIP6. We first evaluated the precipitation performance in the historical period (1959–1988) in the QMs. The change trend and temporal and spatial variations in future precipitation, along with its phase in the QMs, were analyzed in three periods: the short term (2015–2040), the medium term (2041–2070), and the long term (2071–2100). The final results gave an overall understanding of the future precipitation changes in the QMs while providing a scientific reference for understanding future climate and environmental changes in the QMs.

2. Study Area

The QMs are located in the northwest region of China, on the northeast edge of the Qinghai–Tibet Plateau. They span Gansu and Qinghai provinces, with a length of approximately about 800 km from east to west and 200–300 km from north to south [33]. The area extends to the Wu Sheng Ridge in the east, the Altun Mountains in the west, the Hexi Corridor in the north, and the Qadim Basin in the south. The QMs have an average altitude of 4000–4500 m, and the elevation increases from east to west [34,35]. The region is situated in the monsoon water vapor transport channel. The westerly from the far Atlantic mainly affects the central and western parts of the QMs, while the southeast monsoon from the Pacific Ocean and the southwest monsoon from the Indian Ocean affect its eastern region and intersect with the Qinghai–Tibet Plateau circulation system [36]. The QMs represent arid and semi-arid regions of northwest China. In summer, the moisture monsoon extends from north to west, and in winter, it is affected by the dry and cold circulation of Inner Mongolia. Dry and cold wind flows in the northwest, which makes the climate response of the QMs sensitive and increases the precipitation variability [37]. The annual mean air temperature in the QMs is less than 2 °C, and the annual precipitation increases from approximately 200 mm in the low-mountain zone to approximately 500 mm in the high-mountain zone, with high evaporative demand. The ecosystem changes vertically from low to high elevations through dry shrubbery grasslands, forest steppes, subalpine shrubbery meadows, alpine desert meadows, and alpine permafrost and glaciers [38]. According to the Second Glacier Inventory of China [39], there are 2683 glaciers with an area of 1597.81 km² and an ice volume of 84.48 ± 3.13 km³ in the QMs. As an area that is sensitive to changes in climate, the QMs have experienced severe ablations of glaciers, the degradation of permafrost, variations in vegetation, and changes in runoff over recent decades.

To investigate the spatial diversity, longitudes of 101°E and 98°E were selected as the boundaries to divide the eastern, middle, and western portions of the QMs, which was also suggested by Chen et al. [40]. In Figure 1, I, II and III represent the three subregions of the eastern, middle, and western area of the QMs, respectively.

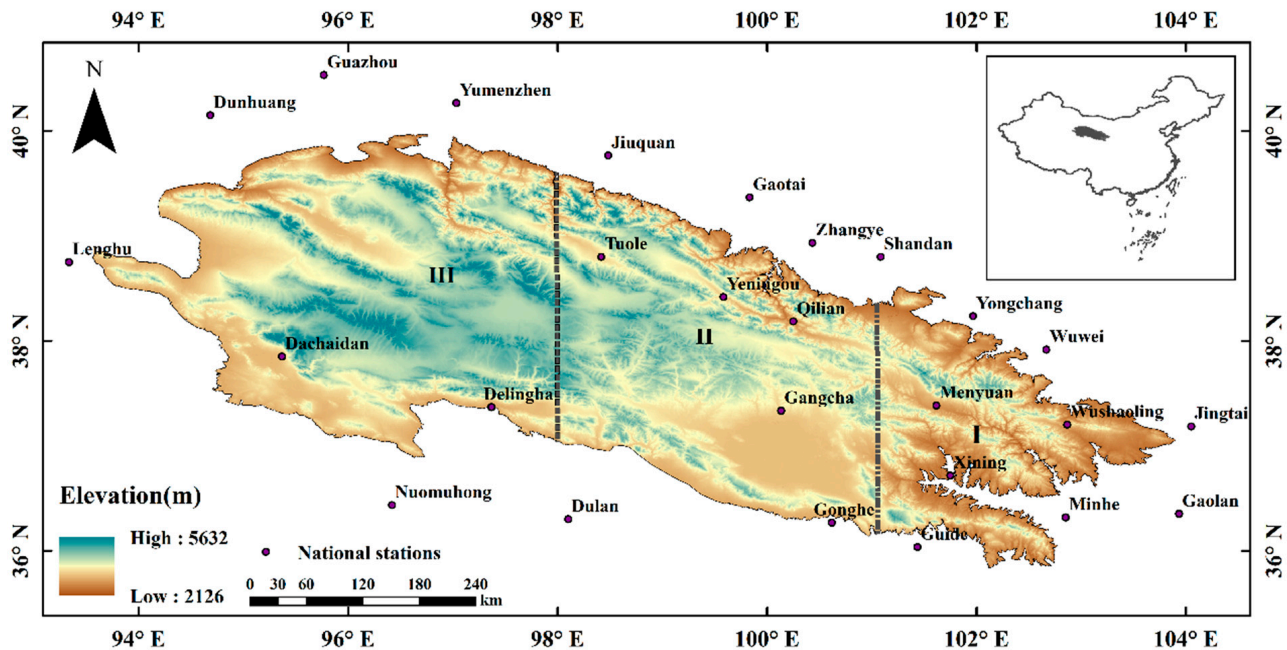


Figure 1. Study area and locations of the meteorological stations (black dots).

3. Data and Methods

3.1. Precipitation Data

The CMIP6 (<https://esgf-node.llnl.gov/search/cmip6/>, accessed on 6 September 2022) data encompass multiple scenarios. Among these, historical scenarios (1959–1988) and four typical future scenarios (2015–2100) were selected for this study. These were SSP126, SSP245, SSP370, and SSP585, representing sustainable pathways, intermediate pathways, regional competitive pathways, and fossil-fuel-based development pathways, respectively [26,41]. The GCMs were selected from CMIP6 based on their availability under r1i1p1f1 initial conditions. Concurrently, this study used 21 CMIP6 models from different countries and research institutions; these have different spatial resolutions, as shown in the basic information presented in Table 1. The time resolution of CMIP6 used in this study was the monthly scale. The precipitation unit for CMIP6 is $\text{kg}\cdot\text{m}^{-2}\cdot\text{s}^{-1}$. Since the time resolution of CMIP6 used in this study was the monthly scale, the unit of precipitation was converted to mm.

CMIP6 combines and coordinates various modeling activities under a single framework, which reduces the computational burden and establishes common practices for producing and analyzing large volumes of model outputs. CMIP6 encourages the adoption of data standards (management structure and metadata) and establishes specifications for the model output of data [42]. This promotes data homogenization.

In this study, the precipitation of the reanalysis dataset ERA5 was used to evaluate the CMIP6.

The meteorological station observations of the QMs from 1959 to 1988 in the daily dataset (V3.0) released by the National Meteorological Information Center were also used, and detailed information regarding this station is shown in Table 2.

Table 1. Basic information for the 21 models of CMIP6.

Number	Model Name	Country	Research Institute	Resolution (km)
1	ACCESS-CM2	Australia	CSIRO-ARCCSS	250
2	ACCESS-ESM1-5	Australia	CSIRO	250
3	AWI-CM-1-1-MR	Germany	AWI	100
4	BCC-CSM2-MR	China	BCC	100
5	CESM2	America	NCAR	100
6	CESM2-WACCM	America	NCAR	100
7	CMCC-CM2-SR5	Italy	CMCC	100
8	CMCC-ESM2	Italy	CMCC	100
9	CNRM-CM6-1-HR	France	CNRM-CERFACS	50
10	CNRM-ESM2-1	France	CNRM-CERFACS	250
11	EC-Earth3	Europe	EC-Earth-Cons	100
12	EC-Earth3-Veg	Europe	EC-Earth-Cons	100
13	EC-Earth3-Veg-LR	Europe	EC-Earth-Cons	100
14	FGOALS-f3-L	China	CAS	100
15	GFDL-ESM4	America	NOAA-GFDL	100
16	KACE-1-0-G	Korea	NIMS-KMA	250
17	MIROC6	Japan	MIROC	250
18	MPI-ESM2-HR	Germany	MPI-M	100
19	MRI-ESM2-0	Japan	MRI	100
20	NorESM2-MM	Norway	NCC	100
21	TaiESM1	China	AS-RCEC	100

Table 2. Information about the meteorological stations of the QMs.

Station	Lat (°N)	Lon (°E)	Altitude (m)	Station	Lat (°N)	Lon (°E)	Altitude (m)
Dunhuang	40.15	94.68	1139.0	Dachaidan	37.85	95.37	3173.2
Guazhou	40.53	95.77	1170.9	Delingha	37.37	97.37	2981.5
Yumenzhen	40.27	97.03	1526.0	Gangcha	37.33	100.13	3301.5
Jiuquan	39.77	98.48	1477.2	Menyuan	37.38	101.62	2850.0
Gaotai	39.37	99.83	1332.2	Wushaoling	37.20	102.87	3045.1
Lenghu	38.75	93.33	2770.0	Jingtai	37.18	104.05	1630.9
Tuole	38.80	98.42	3367.0	Numuhong	36.43	96.42	2790.4
Yeniugou	38.42	99.58	3320.0	Dulan	36.30	98.10	3191.1
Zhangye	38.93	100.40	1482.7	Gonghe	36.27	100.32	2835.0
Qilian	38.13	100.20	2787.4	Xining	36.72	101.75	2295.2
Shandan	38.80	101.08	1764.6	Guide	36.03	101.43	2237.1
Yongchang	38.23	101.97	1976.9	Minhe	36.32	102.85	1813.9
Wuwei	37.92	102.67	1531.5	Gaolan	36.35	103.93	1668.5

3.2. Methods

Based on the meteorological stations, 21 models of CMIP6 were analyzed and evaluated in the historical scenario.

The observational data from the meteorological station in the QMs were processed using the monthly scale. Concurrently, the data of CMIP6 were converted to mm, unifying them with the observational data from the QM meteorological station. The 21 models of CMIP6 were then evaluated through the observed data using the correlation coefficient (r), root mean square error (RMSE), standard deviation (STD), and absolute deviation (BIAS) as follows:

$$r = \frac{\sum_{i=1}^n (X_i - \bar{X})(Y_i - \bar{Y})}{\sqrt{\sum_{i=1}^n (X_i - \bar{X})^2} \sqrt{\sum_{i=1}^n (Y_i - \bar{Y})^2}} \quad (1)$$

$$RMSE = \sqrt{\frac{\sum_{i=1}^n (X_i - Y_i)^2}{n}} \quad (2)$$

$$STD = \sqrt{\frac{\sum_{i=1}^n (Y_i - \bar{Y})^2}{n}} \quad (3)$$

$$BIAS = \frac{\sum_{i=1}^n (Y_i - X_i)}{n} \quad (4)$$

Here, X is the observed value and Y is the simulated value. The range of r is -1 – 1 . A significance test ($p < 0.05$) was also performed. In addition, the linear trend method was used to analyze the annual precipitation trend over time in the QMs. The World Meteorological Organization stipulates that a climate state should be viewed as a 30-year average, which is often used to assess climate in order to better observe climate change characteristics [43–45]. Therefore, this study divided the period up to the end of the century into 2015–2040 in the short term, 2041–2070 in the medium term, and 2071–2100 in the long term.

Since the spatial grid resolution of each model of CMIP6 is different, this study adopted the bilinear interpolation method to interpolate the CMIP6 data to a unified resolution of $0.1^\circ \times 0.1^\circ$. Due to the differences in resolution between the grids, some information may be lost [46]. However, previous studies have used similar methods and reported that the data quality was largely unaffected [47,48].

The flow chart of this study is as follows (Figure 2):

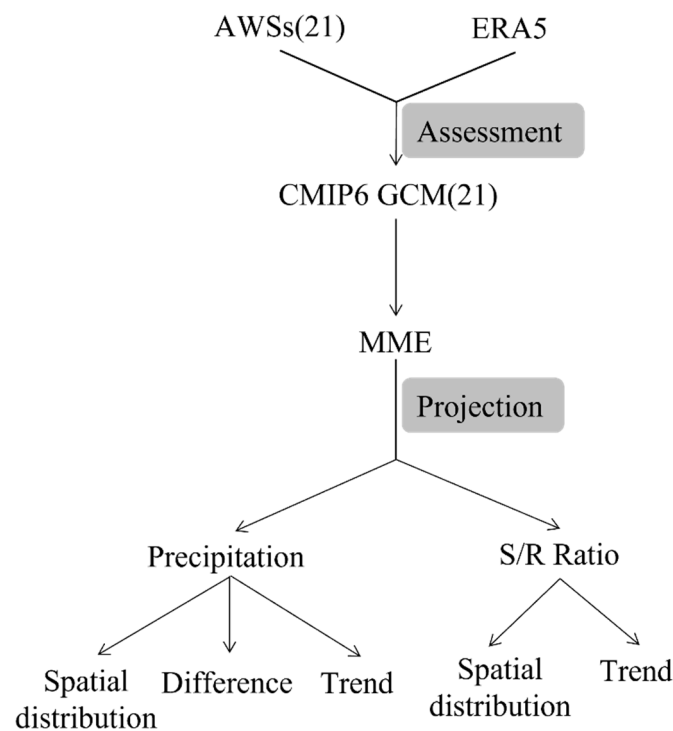


Figure 2. Flow chart of this study.

4. Results

4.1. CMIP6 Model Performance

To better evaluate CMIP6, we compared the models with ERA5 and AWSs (Table 3), and the r between most models and the observational data reached 0.5. Only nine of the 26 stations failed the significance test ($p < 0.05$) (Table S1). Notably, the r of the four models of CESM2, CESM2-WACCM, MIROC6, and NorESM2-MM was as high as 0.6, which indicated a strong correlation. Many studies have shown that the GCMs have good applicability in the Qinghai–Tibet Plateau [49]. KACE-1-0-G had the worst correlation

coefficient (around 0.27), indicating a weak correlation. The r of MME was around 0.67. The r of ERA5 was as high as 0.81, which shows a strong correlation.

Table 3. The r , RMSE, STD, and BIAS of 21 models of CMIP6, MME and ERA5 with meteorological station data.

	R	RMSE	STD	BIAS
ACCESS-ESM1-5	0.39	32.55	26.29	18.22
ACCESS-CM2	0.39	35.10	24.97	22.73
AWI-CM-1-1-MR	0.36	30.87	27.68	14.18
BCC-CSM2-MR	0.47	38.96	32.20	26.49
CESM2-WACCM	0.61	56.54	54.14	36.86
CESM2	0.63	54.47	52.29	35.91
CMCC-CM2-SR5	0.56	59.13	51.58	42.32
CMCC-ESM2	0.55	57.45	50.15	40.71
CNRM-CM6-1-HR	0.54	26.12	29.11	9.25
CNRM-ESM2-1	0.49	38.59	40.51	19.50
EC-Earth3-Veg-LR	0.50	24.72	26.11	10.86
EC-Earth3-Veg	0.51	22.43	24.43	9.74
EC-Earth3	0.52	23.18	25.33	10.35
FGOALS-f3-L	0.47	25.74	24.94	10.46
GFDL-ESM4	0.60	34.57	35.14	21.59
KACE-1-0-G	0.27	32.62	27.38	13.92
MIROC6	0.62	49.69	44.15	36.83
MPI-ESM1-2-HR	0.33	32.41	28.60	14.99
MRI-ESM2-0	0.42	30.89	26.15	17.93
NorESM2-MM	0.63	46.32	46.78	29.15
TaiESM1	0.56	45.77	43.15	30.16
MME	0.67	29.56	28.00	22.48
ERA5	0.81	27.80	34.11	18.41

Throughout the QMs, the RMSE ranged from 22.43 to 59.13 mm. The minimum value occurred in EC-Earth3-Veg and the maximum value was in CMCC-CM2-SR5. The RMSE of MME was 29.56 mm, and the RMSE of ERA5 was 27.80 mm.

In terms of BIAS, the range was between 9.25 and 42.32 mm. The maximum occurred in CMCC-CM2-SR5 and the minimum occurred in CNRM-CM6-1-HR. Secondly, the BIAS results of EC-Earth3-Veg-LR, EC-Earth3-Veg, EC-Earth3, and FGOALS-f3-L were also small values, at 10.86, 9.74, 10.35, and 10.46 mm, respectively. The BIAS of MME was 22.48 mm, and the BIAS of the reanalysis data was 18.41 mm.

In terms of STD, the models of STD and BIAS behave similarly. The range was between 24.43 and 54.14 mm. The maximum value occurred in CESM2-WACCM and the minimum value occurred in EC-Earth3-Veg. Additionally, as with the absolute error, EC-Earth3-Veg-LR, EC-Earth3-Veg, and EC-Earth3 performed better, with smaller errors of 26.39, 25.57, and 25.94 mm, respectively. The STD of MME was 28.00 mm, and the STD of ERA5 was 34.11 mm.

According to the time series of monthly mean precipitation comparison between MME and AWSs from 1959 to 1988 in the QMs and subregions (Figure 3), the variation trend in MME and AWSs curves was basically the same in the whole QM region and in the east, middle, and west regions. However, the MME showed a certain wet bias, especially in summer (Figure 3). In the entire QM region, the average difference was 22.48 mm, while it was 28.12, 23.16, and 13.58 mm in the eastern, middle, and western regions, respectively. One of the factors affecting this deviation is the convection scheme. Convection schemes affect monsoon modeling, resulting in wet bias (see Discussion in Section 5.2). Another possible factor for the wet bias was the sparse distribution of stations in the QMs. Most of these stations are located in the valleys of the QMs, and there are elevation errors between them and the grid points of the model, which may lead to an underestimation of precipitation [50]. Especially in the western region, precipitation decreases gradually with

increasing altitude, and the whole layer of atmospheric water vapor is mainly concentrated below 5000 m.

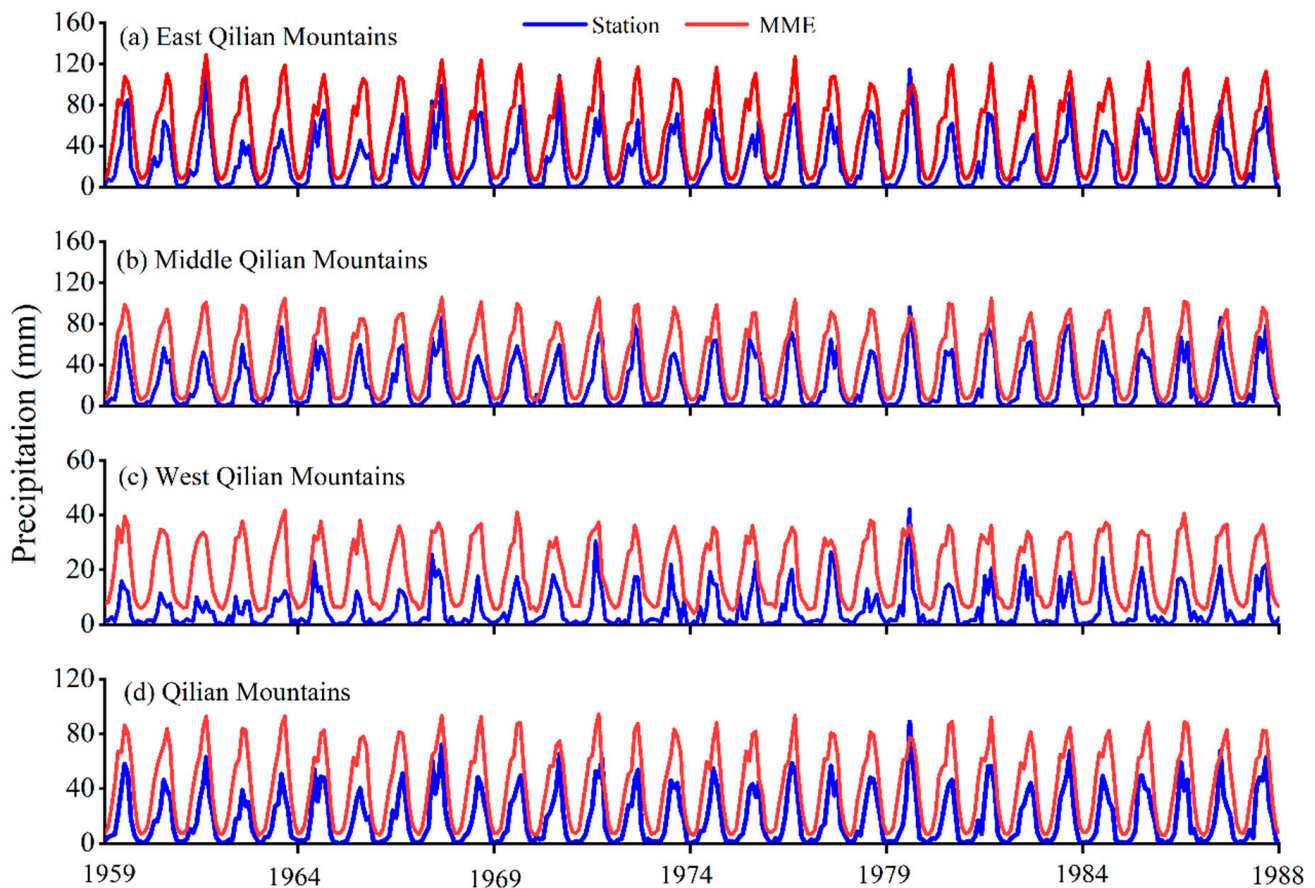


Figure 3. Time series of monthly mean precipitation comparison between MME and AWSs from 1959 to 1988 in the QMs and subregions.

From the data we have analyzed, we found that (Figure 4) MME simulated the spatial distribution characteristics of decreasing precipitation from the southeast to northwest QM, which is in agreement with Qiang Fang’s research [51]. As an important place in the atmospheric water cycle in the northwestern arid zone [52], its water vapor transport process is affected by the westerly wind mode. Moreover, the water vapor content in the eastern and western parts of the QMs differs significantly due to the blocking effect of the Qinghai–Tibet Plateau [53]. Figure 4 shows a good agreement between MME and ERA5 over the QMs. The average seasonal precipitation of MME in spring, summer, autumn and winter was 130.07, 224.62, 95.96, and 29.07 mm, respectively, and that of ERA5 was 98.57, 280.77, 96.85, and 22.64 mm, respectively. There is a precipitation center in the eastern QMs with an annual precipitation of more than 400 mm. The distribution of precipitation in this area is consistent with the trend in the mountain, which shows that the QMs play an important role in the precipitation in this area and the surrounding areas. Previous studies have shown that the cyclonic vorticity generated by topography is an important cause of the precipitation in mountainous areas, which leads to the cyclonic convergence at a low altitude [40]. The QMs are composed of several parallel mountain ranges and valleys in a northwest–southeast direction, and the westerly airflow is forced to rise when blocked by the mountain ranges. Therefore, the warm and humid southerly airflow can be transported northward along the valley passages [54]—especially in the summer, when the southeast monsoon from the Pacific Ocean significantly increases water vapor the thermal unevenness of the terrain becomes quite obvious. Additionally, the cyclonic convergence of the low-level atmosphere and the concentration of water vapor and heat can stimulate

the release of unstable energy, which is conducive to the unstable development of vertical circulation and leads to the onset of precipitation. The rise of the spokes induced by the terrain is limited to the lower layers, but the release of latent heat from the atmosphere can strengthen the warming of the middle and upper floors and the dispersion of the upper floors. This is conducive to the upward extension and addition of the vertical circulation of the strong terrain, forming feedback, and eventually leading to a strong increase in precipitation [55].

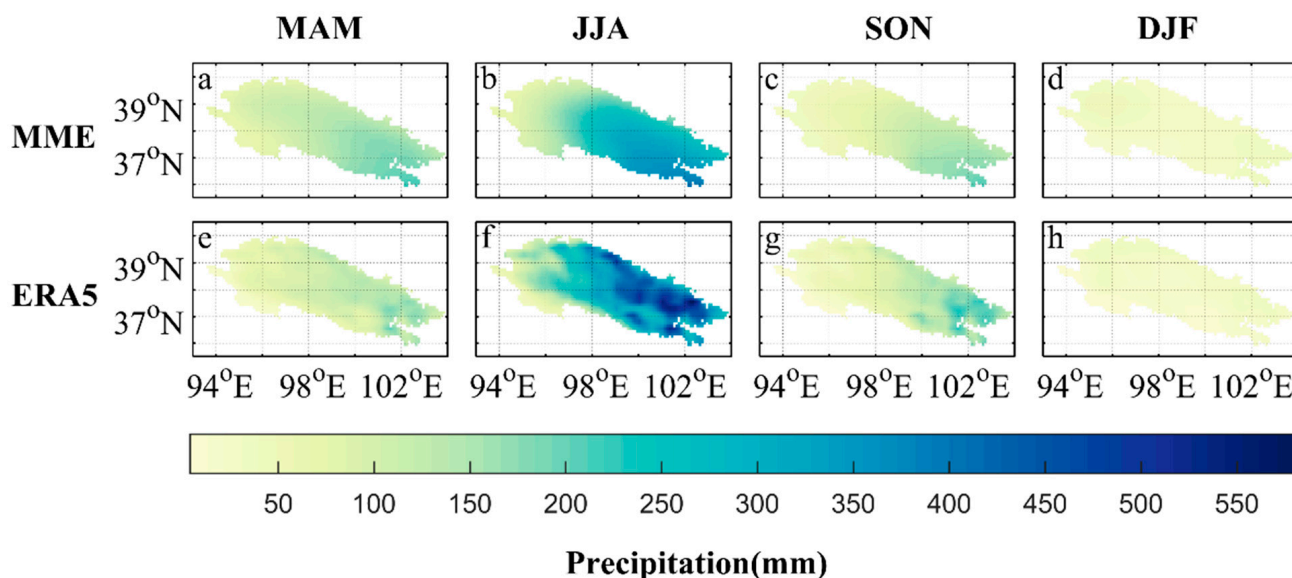


Figure 4. Seasonal average precipitation from 1959 to 1988 from MME (a–d) and ERA5 (e–h) for spring (MAM), summer (JJA), autumn (SON) and winter (DJF).

Figure 5 shows the average spatial distribution of the annual precipitation differences between 21 models of CMIP6 (a–u), MME (v) and ERA5 in the QMs during the period of 1959–1988. The results showed that the maximum difference between the 21 models of CMIP6 and ERA5 was 739.28 and the minimum was -606.59 mm. The maximum difference between MME and ERA5 was 396.36 and the minimum was -410.09 mm. MME could simulate the characteristics in the central region of the QMs, and the difference ranged from -100 to 100 mm. In the northern and northeastern regions, MME showed a dry deviation, especially in the northern region, with a maximum difference of 396.36 mm compared with ERA5. At the southern edge of the QMs, MME also showed a significant wet deviation, with a maximum value of 410.09 mm in the area south of Qinghai Lake. In the Qinghai Lake area, there was a dry deviation opposite to that observed in the surrounding area. Figure 6 shows the flood season, July and August, in the QMs. Precipitation could reach more than 80 mm, which was mainly due to the influence of the southeast monsoon from the Pacific Ocean, which was consistent with Chen’s results [40]. In the context of global warming, the strengthening of atmospheric circulation processes and the increase in stratum humidity play an important role in precipitation in northwest China, especially regarding the impact of horizontal diversion [45,46]. Furthermore, in terms of the difference between MME and ERA5, ERA5 exhibits an overestimation of precipitation for most of the year (especially summer and autumn), which is consistent with previous research. This is related to the composition of the dataset itself. The MME has a flatter curve, which is due to the fact that the MME could average out both high and low values. This can be seen in Figure S6, where the curve for the single model CESM2 and the curve for ERA5 are both more volatile.

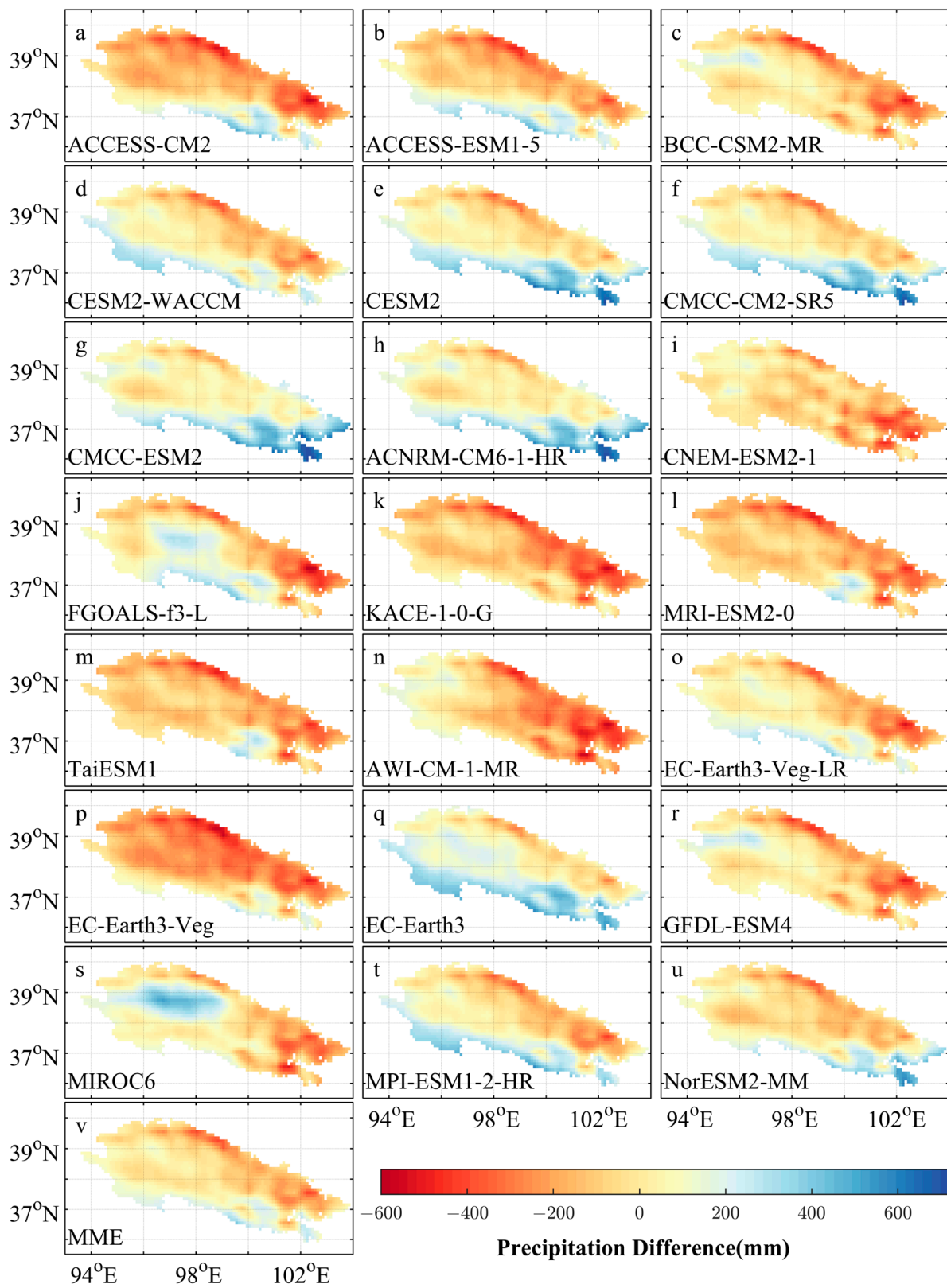


Figure 5. Average annual precipitation differences (mm) between the 21 models of CMIP6 (a–u), MME (v), and ERA5 during the period 1959–1988.

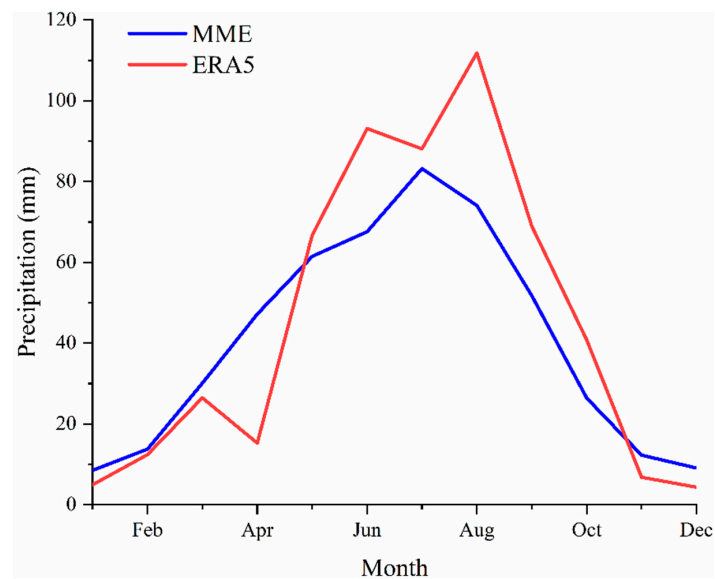


Figure 6. Annual cycles of mean monthly precipitation from MME (blue line) and ERA5 (red line) during the period 1959–1988.

In terms of the time series of annual total precipitation in MME and ERA5 from 1959 to 1988 (Figure 7), precipitation in the QMs behaved relatively smoothly until the abrupt change in the 1990s. The climatic tendency rate of MME was $-2.01 \text{ mm} \cdot 10\text{a}^{-1}$, which is slightly lower than that of ERA5 ($2.82 \text{ mm} \cdot 10\text{a}^{-1}$). At the same time, it could be concluded that some models showed wet deviation and some models showed dry deviation. Furthermore, MME was basically consistent with the precipitation trend in ERA5, simulating the linear change trend of annual precipitation in the QMs.

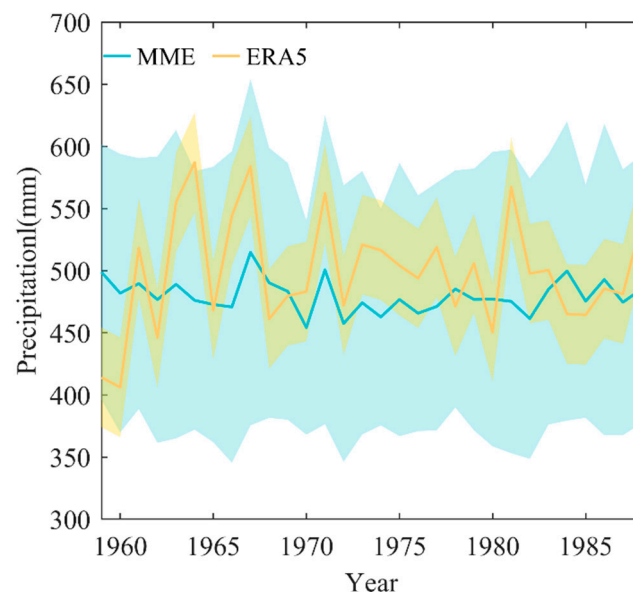


Figure 7. Time series of annual total precipitation from MME (blue line) and ERA5 (yellow line) during the period 1959–1988 (the shaded part represents one standard deviation).

In summary, regarding r , RMSE, STD, BIAS, and the spatial and temporal distribution of precipitation, MME could effectively reduce the uncertainty of CMIP6 and significantly improve the accuracy of the research [56]. Therefore, MME was used to estimate and predict the precipitation.

4.2. Projections of Changes in Precipitation in the 21st Century

Estimating the future trend in annual precipitation in the QMs was one of the prime objectives of this study. Therefore, the four typical future scenarios of SSP126, SSP245, SSP370, and SSP585 were selected for analysis. In addition, the spatial variation characteristics and temporal trends of precipitation in the QMs from 2015 to 2100 were analyzed using MME.

4.2.1. Spatial Distribution of Precipitation

This study projected the spatial distribution of precipitation in the QMs by the end of the century (2015–2100) in four scenarios (Figure 8a–d). The difference shown in the pictures is not particularly obvious, so we produced a spatial distribution map (Figure 8e–p) of the differences between the near-term (2015–2040), medium-term (2041–2070) and long-term (2071–2100) future precipitation and the historical precipitation in four scenarios (SSP126, SSP245, SSP370, SSP585). Overall, in the four scenarios, the spatial distribution of precipitation still showed a decrease from southeast to northwest. Regarding the different emission scenarios, the increasing trend in precipitation in the SSP126 scenario was not obvious, continuing the characteristics of the historical period. The average annual precipitation was 515.76 in the short term (2015–2040), 544.34 in the medium term (2041–2070), and 548.26 mm in the long term (2071–2100). The average annual precipitation in most areas was concentrated between 220 and 950 mm. In the SSP245 scenario, the average annual precipitation in the near term, medium term, and long term was 508.78, 538.82, and 532.70 mm, while the average annual precipitation was concentrated between 240 and 950 mm. In the SSP370 scenario, the average annual precipitation in the short term, medium term, and long term was 510.84, 541.36, and 581.560 mm, respectively, and the average annual precipitation was concentrated between 260 and 950 mm. In the SSP585 scenario, the average annual precipitation in the short term, medium term, and long term was 520.16, 558.32, and 610.14 mm, respectively, and the average annual precipitation was concentrated between 260 and 1000 mm.

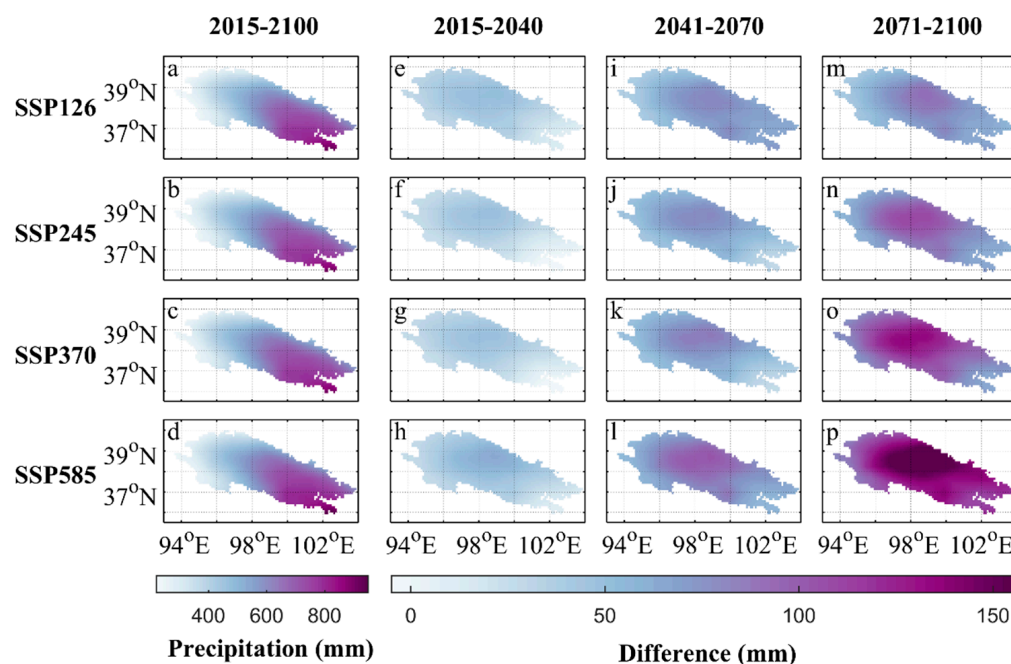


Figure 8. Average annual precipitation during the period 2015–2100: SSP126 (a), SSP245 (b), SSP370 (c), and SSP585 (d) and differences between four different SSPs (2015–2040, 2041–2070, and 2071–2100) and the historical period (1959–1988): SSP126 (e,i,m), SSP245 (f,j,n), SSP370 (g,k,o), and SSP585 (h,l,p).

It was found that precipitation in the QMs exhibited a weak increasing trend over time, but this is not obvious in the figure. According to the data, the precipitation increase was the most obvious in the SSP585 scenario. As such, it is necessary to control carbon emissions.

4.2.2. Precipitation Difference

The spatial distribution of the differences in annual precipitation between the projected and historical periods in future scenarios (Figure 8e–p) further showed the overall change in average annual precipitation. Based on different emissions scenarios, the annual average precipitation showed an overall trend of increasing when compared with the historical period. In this comparison, in the SSP126 scenario, the average increase in short-, medium-, and long-term annual precipitation was 28.94, 57.52, and 61.44 mm, respectively. Compared with the historical period, in the SSP245 scenario, the average increase in short-term (2015–2040), medium-term (2041–2070), and long-term (2071–2100) annual precipitation was 21.96, 52.00, and 75.89 mm, respectively. In the SSP370 scenario, compared with the historical period, the short-, medium- and long-term annual precipitation increased by 24.02, 54.54, and 94.73 mm, respectively. In the SSP585 scenario, compared with the historical period, the average increase in short-term (2015–2040), medium-term (2041–2070), and long term (2071–2100) annual precipitation was 33.35, 71.50, and 123.32 mm, respectively. At the same time, the increase in annual precipitation was particularly obvious in the north of the central QMs, especially in the SSP370 and SSP585 scenarios, where the maximum increase reached 124.84 and 155.91 mm, respectively.

The average seasonal precipitation differences between the SSPs and historical periods (Table 4 and Figure 9) showed that in the four scenarios, the future precipitation in each season in the QMs exhibits an increasing trend compared with the historical period. The increases, which were especially pronounced in summer, were 21.52, 20.48, 23.00, and 29.24 mm, respectively. Summer showed the largest increase in the four seasons, because the precipitation in the QMs is mainly concentrated in the summer; meanwhile, the winter precipitation had the lowest values and increased the least with values of 3.96, 5.17, 6.35, and 7.77 mm.

Table 4. Average seasonal precipitation differences between SSPs and historical periods.

Difference (mm)	MAM	JJA	SON	DJF
SSP126	17.95	21.52	13.13	4.78
SSP245	18.48	20.48	13.43	5.99
SSP370	20.89	23.00	15.39	7.17
SSP585	25.53	29.24	21.83	8.59

Therefore, based on the different emissions scenarios (CO₂, CH₄, N₂O, and other gas concentrations), annual precipitation also tends to increase as emissions increase. Precipitation could affect CO₂ emissions by affecting plant growth and soil conditions. Rainfall is necessary for plant growth and the removal of carbon from the atmosphere through photosynthesis. In arid regions, plant growth may be restricted due to water scarcity, resulting in reduced carbon uptake. In addition, precipitation may affect soil moisture levels, which play a vital role in determining the rate of soil CO₂ emissions. Dry soils tend to release more carbon dioxide than wet soils, so changes in precipitation patterns could affect how quickly carbon dioxide is released from the ground. Overall, it is clear that there is a complex interaction between precipitation and carbon dioxide emissions. Understanding these relationships is critical to implementing effective climate change mitigation strategies and adapting to the impact of changing weather patterns.

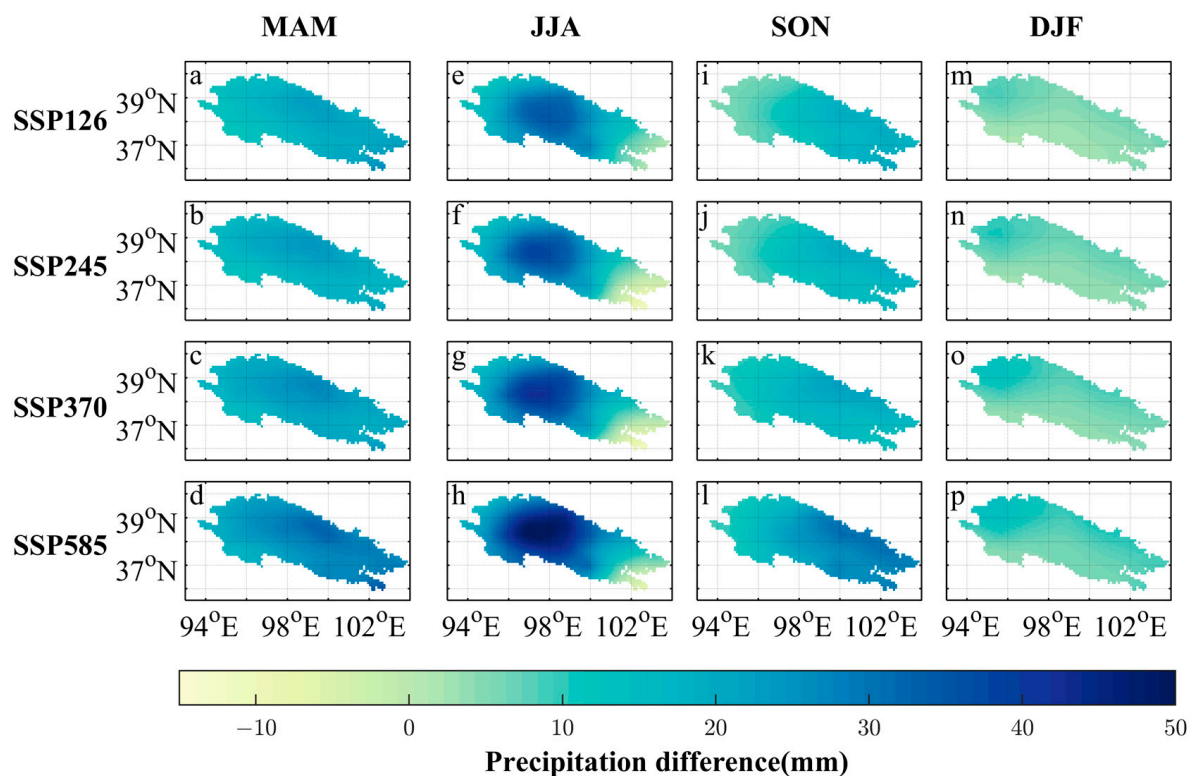


Figure 9. Average differences in seasonal precipitation between four different SSPs (2015–2100) and the historical period (1959–1988): MAM (a–d), JJA (e–h), SON (i–l), DJF (m–p).

According to Figure 9, in all scenarios, the recent precipitation increase was not significant, but the long-term precipitation increase was obvious, especially in the SSP585 scenario. This suggests that carbon emissions have a significant effect on precipitation.

4.2.3. Precipitation Trends

The spatial distribution of the precipitation trend in each season (Figure 10) and the linear trend (Figure 11) of annual precipitation compared with the historical period in different future scenarios also showed that annual precipitation in the QMs had always shown an increasing trend from 2015 to 2100. Since the precipitation in the QMs is mainly concentrated in the summer (Table 5), the increasing trend in summer was 1.85, 2.77, 3.03, and 4.45 $\text{mm}\cdot 10\text{a}^{-1}$ for each of the four scenarios. This was much larger than that observed in winter (0.35, 0.78, 1.27, and 1.94 $\text{mm}\cdot 10\text{a}^{-1}$, respectively). In addition, due to global warming, the growth trend in spring precipitation was also more obvious with values of 1.80, 3.12, 4.19, and 5.06 $\text{mm}\cdot 10\text{a}^{-1}$. Finally, for all seasons in the four scenarios, with the increase in the concentrations of CH_4 , N_2O , and other gases, the precipitation growth trend was also more pronounced.

Table 5. Trends in average seasonal precipitation.

Trend ($\text{mm}\cdot 10\text{a}^{-1}$)	MAM	JJA	SON	DJF
SSP126	1.80	1.85	1.72	0.35
SSP245	3.12	2.77	2.46	0.78
SSP370	4.19	3.03	3.73	1.27
SSP585	5.06	4.45	4.69	1.94

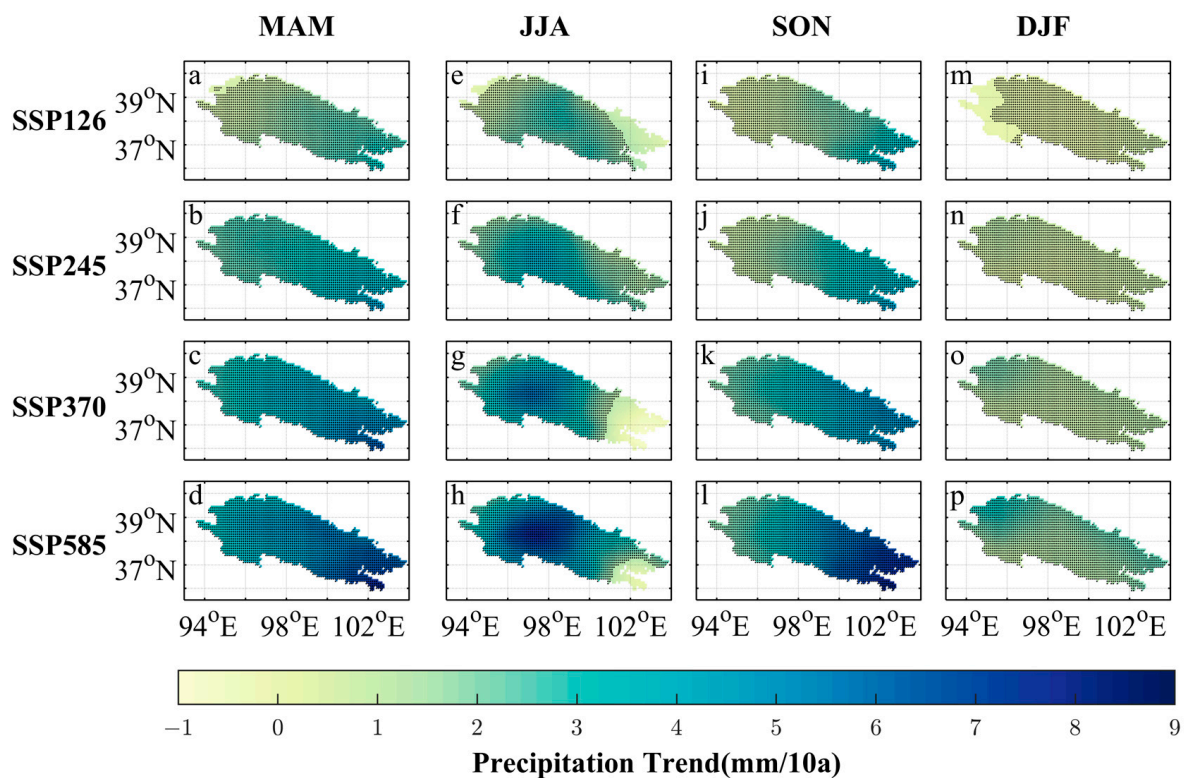


Figure 10. Trends in the average seasonal precipitation from 2015 to 2100 from the MME: MAM (a–d), JJA (e–h), SON (i–l), DJF (m–p) (the black dots represent the points that pass the significance test at $p < 0.05$).

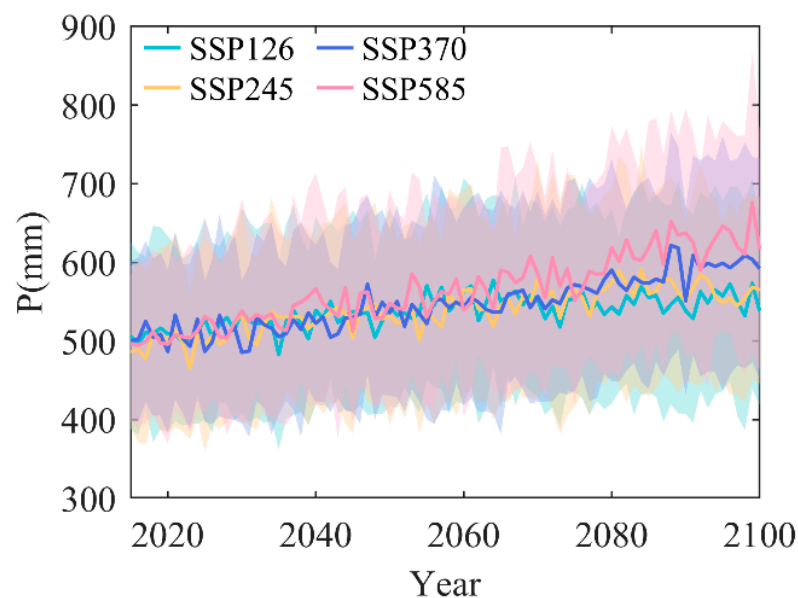


Figure 11. Time series of annual total precipitation from 2015 to 2100 from the MME (the shaded part represents one standard deviation).

These results are also consistent with a previous study, which reported that in different future scenarios, the climate will be warm and humid due to the emission of greenhouse gases [57]. In addition to global warming, another reason for this increase may be that the intensity of the Somali equatorial air flow had periodically become stronger [58]. From the perspective of atmospheric circulation and water vapor transport, this air flow and the eastern precipitation of northwest China have a significant correlation: when the Somali

equatorial air flow strengthens, the East Asia region's abnormal easterly wind appears, and, at the same time, this can easily form the 500 hPa circulation type in Eurasia. This circulation type would increase precipitation in northwest China [58].

4.3. Changes in the Snow-to-Rain Ratio in the 21st Century

Based on the above analysis of the spatial distribution characteristics and temporal trends in precipitation in the QMs, keeping the importance of precipitation in northwest China in mind, this study subdivided precipitation into snowfall and rainfall. In addition, the temporal and spatial distribution and change trends in historical and future annual snowfall, rainfall and the snow-to-rain ratio in the QMs were further explored (Figure 12). As the CESM2-WACCM data were missing, the following analysis used data from 20 models.

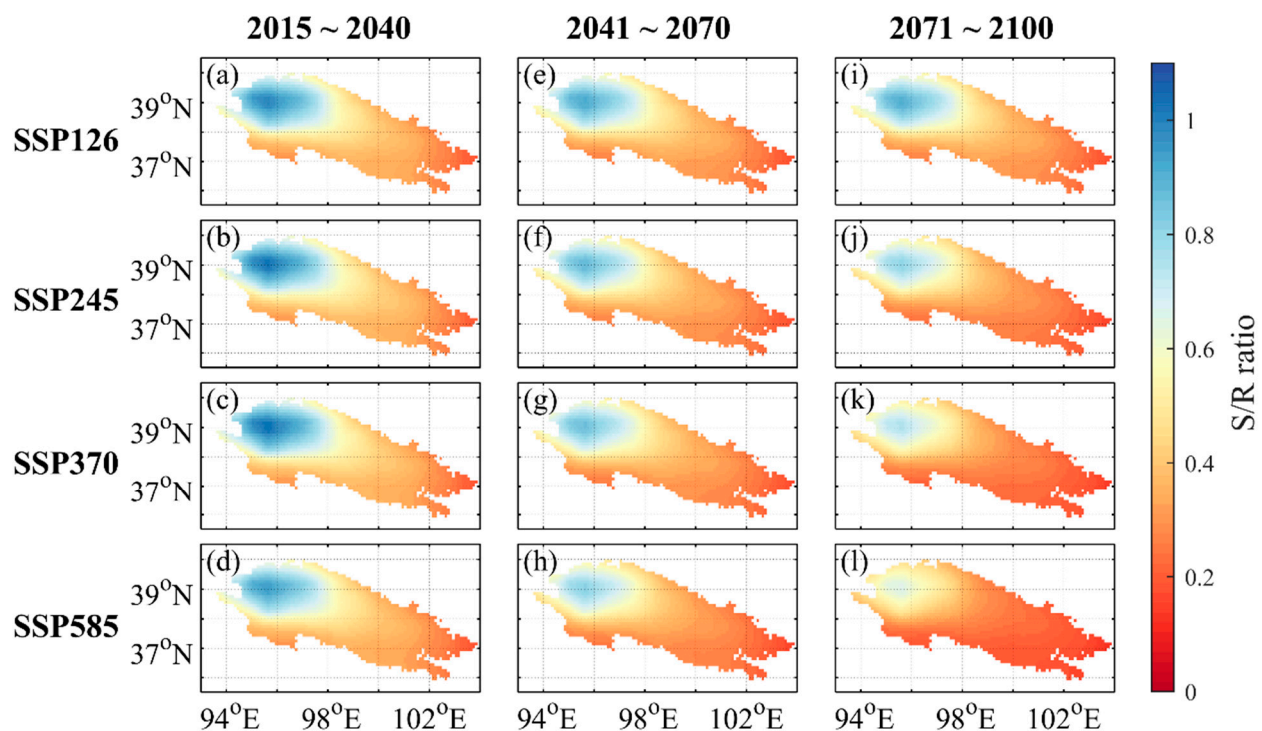


Figure 12. Average annual snow-to-rain (S/R) ratio (2015–2040, 2041–2070, and 2071–2100) from MME: SSP126 (a–c), SSP245(d–f), SSP370 (g–i), and SSP585 (j–l).

Figure 12 shows that the snow-to-rain ratio was between 0.1 and 1.1, snowfall was predominant in the northwest and rainfall was predominant in the southeast. With the increase in emissions, the snow-to-rain ratio showed a downward trend. In addition, the spatial distribution of the differences between projected and historical snowfall over the short, medium and long-term periods from 2015 to 2100 (Figure S2) showed an overall trend of decreasing. This decreasing trend was significantly accelerated with increasing emission levels. At the same time, the spatial distribution of the differences between projected and historical rainfall (Figure S3) showed an overall increase compared with the historical period.

From 2015 to 2100, in the four scenarios, the average seasonal snow-to-rain ratio of the QMs (Figure 13) was the highest in winter, with values of 16.77, 17.14, 15.82, and 15.26. This is mainly because the temperature in winter is low in this region, causing snow to be mainly concentrated in the winter. The ratio of snow to rain was lowest in the summer, with values of 0.04, 0.04, 0.03, and 0.03, due to the high temperatures in summer, meaning that this season mainly experiences liquid precipitation. In addition, the numerical value indicated that with the increase in emissions, the ratio of snow to rain showed an insignificant downward trend in both winter and summer.

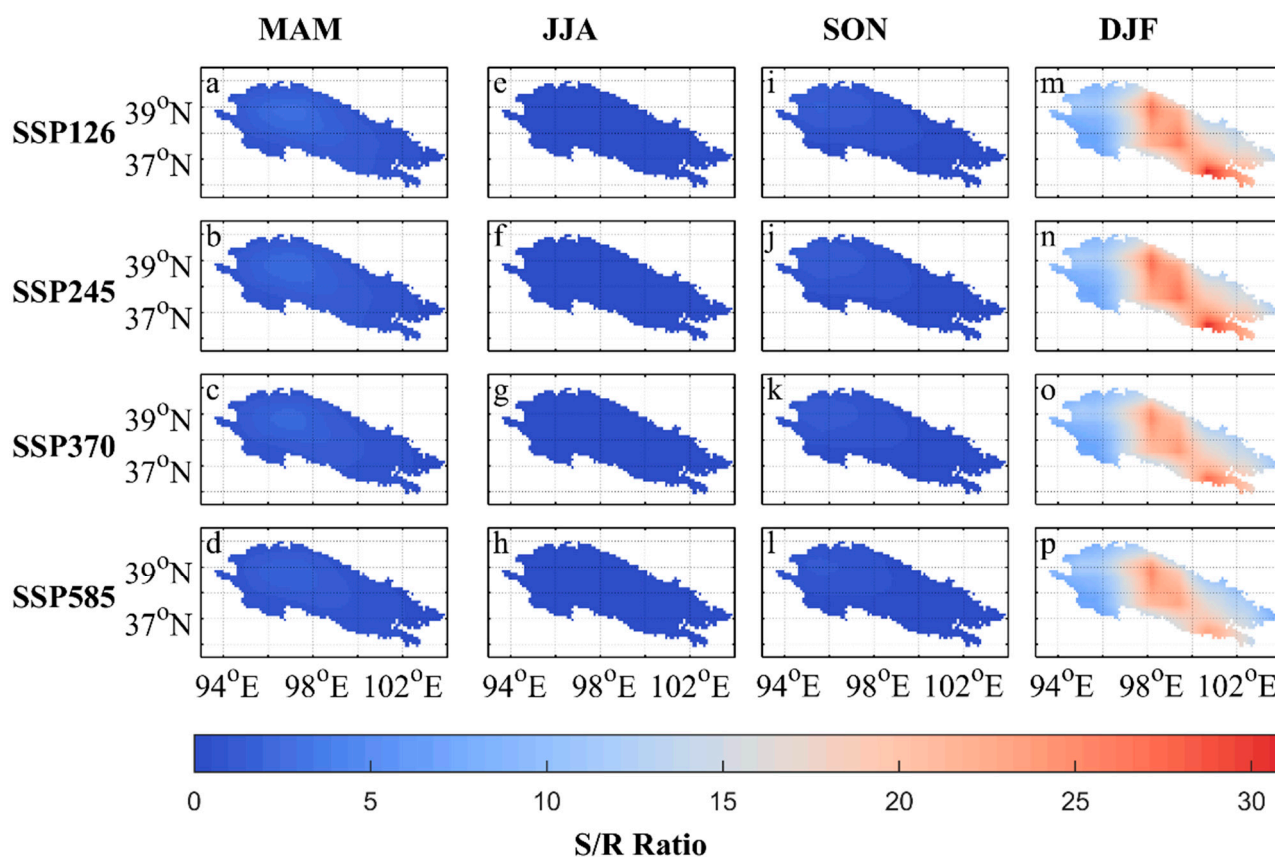


Figure 13. Average seasonal S/R ratio (2015–2100): MAM (a–d), JJA (e–h), SON (i–l), and DJF (m–p).

Compared with the historical period, the spatial trend (Figure 14) and linear trend (Figure 15a) of annual snowfall in the future scenarios also showed that during the period from 2015 to 2100, most of the annual snowfall exhibited a decreasing trend. Meanwhile, the snow/rain ratio climate tendency rate was concentrated in the range of $-10\sim-0.1\text{ mm}\cdot 10\text{a}^{-1}$, and both passed the significance test ($p < 0.05$). In the SSP126, SSP245, SSP370, and SSP585 scenarios, the average annual decrease rate in snowfall in the entire QM area was 0.42 , 2.18 , 3.34 and $4.17\text{ mm}\cdot 10\text{a}^{-1}$, respectively. Additionally, in the four scenarios of SSP126, SSP245, SSP370, and SSP585, the maximum reduction in annual snowfall throughout the entire QM region was 1.65 , 4.99 , 7.27 , and $9.34\text{ mm}\cdot 10\text{a}^{-1}$, respectively. This showed that the snowfall was mainly concentrated in the southeastern and central regions. The reason for this could be that the altitude of the space over the QMs is smaller than that of the northwest Pacific Ocean, resulting in the strengthening of the easterly wind over the QM and the formation of a westward water vapor belt. However, the water vapor flux and temperature were lower than the average state, indicating that the cold and dry air flow was transported to the QMs by the easterly wind, and the water vapor radiated over the QMs, making it difficult for snowfall to form over the QMs [59]. The spatial trend in annual rainfall compared to the historical period in the future scenarios (Figure 14) and linear trend (Figure 15b) also showed that from 2015 to 2100, the annual rainfall in the QMs always exhibited an increasing trend, and the climate tendency rate was between 0 and $-30\text{ mm}\cdot 10\text{a}^{-1}$; both passed the significance test ($p < 0.05$). In the SSP126, SSP245, SSP370, and SSP585 scenarios, the rates of increase in the average annual rainfall in the entire QM region were 6.20 , 11.31 , 5.64 , and $20.41\text{ mm}\cdot 10\text{a}^{-1}$, respectively. Moreover, the maximum increase in annual rainfall in the entire QM region was 11.21 , 18.02 , 20.65 , and $27.93\text{ mm}\cdot 10\text{a}^{-1}$, respectively. The rainfall was mainly concentrated in the southeast and central regions, which is a finding that is basically consistent with the area having decreased annual snowfall. This reflects

the fact that as temperatures increase, the phase change in precipitation is more obvious, changing from solid to liquid precipitation.

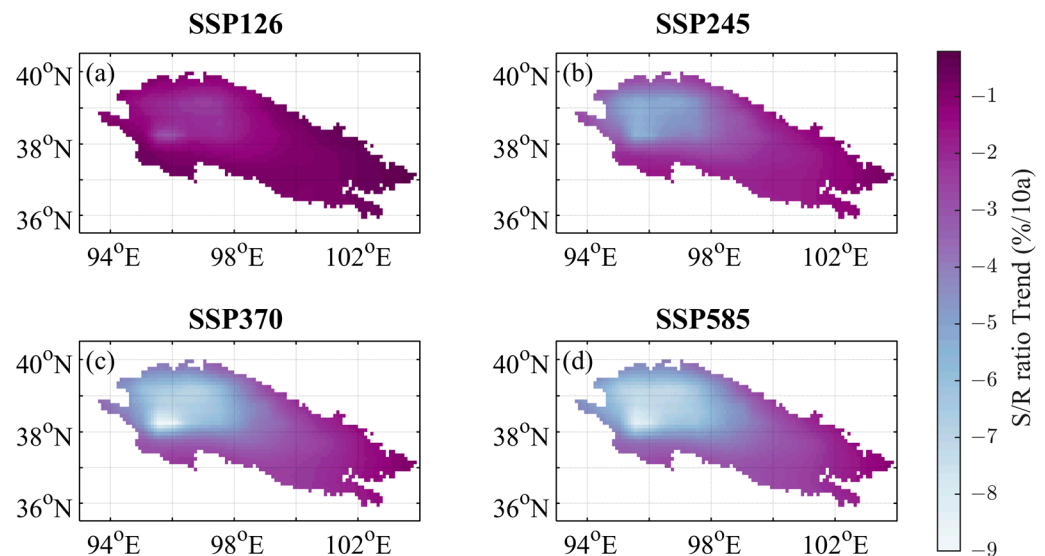


Figure 14. Trends in the S/R ratio during the period 2015–2100 from the MME: SSP126 (a), SSP245 (b), SSP370 (c), and SSP585 (d).

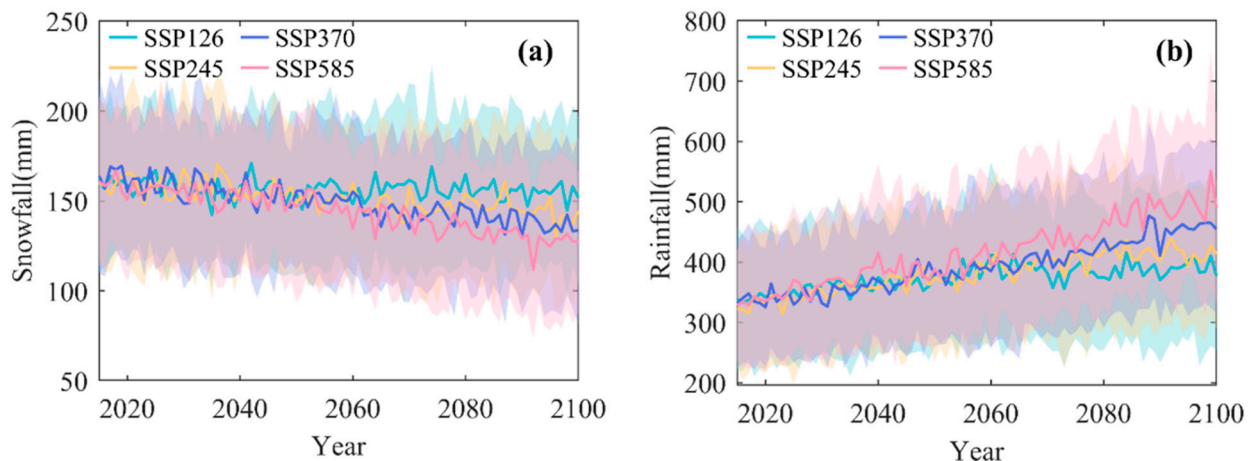


Figure 15. Time series of annual total snowfall (a) and rainfall (b) during the period 2015–2100 from the MME.

This conclusion is in line with Deng’s research [60], which suggests that rising temperatures in places that are already near freezing mean that snow will turn to rain and snowfall will rapidly diminish [60].

5. Discussion

5.1. Factors Affecting Precipitation Changes

This study used 21 models of CMIP6 for the assessment of historical scenarios to estimate the temporal and spatial trends in precipitation from 2015 to 2100. As is shown in Figure 10, precipitation in the QMs showed an increasing trend in the four scenarios. Rainfall (Figure 15a) also showed an increasing trend, while snowfall (Figure 15b) showed a downward trend. There are many glaciers in the high altitude of the QMs, which could be a result of the troposphere being more active under a warming climate. Warm air is more likely to form precipitation in the high-altitude glacial areas of the QMs. At the same time, precipitation is an important factor affecting the change in the mass balance

of glaciers. Some studies have shown that warming and increased precipitation will lead to glacier retreat [61,62]. So, in the context of the climate warming, by the middle and late 21st century, the glaciers of the QMs will undergo significant changes [50].

Previous studies of the QMs focused on temperature and precipitation, but little consideration has been given to radiation and other meteorological variables [63–65]. This is mainly because it is not possible to conduct routine measurements of these variables. In addition to precipitation and temperature, other meteorological variables play an important role in land–air interactions. For example, wind speed strongly affects the transfer of energy, water, and momentum between land and the atmosphere, and the surface radiant flux is the driving force behind the surface energy balance [66]. The amount of precipitation is intimately connected with climate change, which is closely linked to climate drivers such as the Indian Ocean Dipole (IOD), the El Niño Southern Oscillation (ENSO), and the Pacific Decadal Oscillation (PDO). For example, researchers have found that the IOD has an impact on drought episodes over southwest SA relative to the northern parts, and it is mostly affected by variability in the sea surface temperature (SST) [67].

As the material basis of precipitation, water vapor is the primary physical factor used to analyze precipitation changes. At present, there are different views on the sources of water vapor with increased precipitation over this region. Studies have found that the prevailing westerly wind zone west of 102.5°E [68] increased water vapor transport to the northwest after 1987, resulting in increased precipitation [69]. An increase in the height of the 500 hPa potential in the Mongolia–Baikal region triggers abnormal anticyclonic airflow, which weakens the east Asian summer wind [70]. Meanwhile, the North Pacific region is also dominated by abnormal anticyclones, resulting in easterly water vapor transport to the west at high latitudes. Elsewhere, in the western North Pacific, the combination of water vapor and cold dry air leads to an increase in precipitation in the northwest region. However, Xue [71] believed that Xinjiang, the Hexi Corridor, and the eastern part of Qinghai showed obvious water vapor convergence. In addition, abnormal cyclones over central Asia transport water vapor from the Arabian Sea and Indian Ocean along the eastern side of the Iranian Plateau to central Asia. This reduces the amount of water vapor transported to the northwest region, indicating that the increase in precipitation in the northwest region mainly comes from the Pacific Ocean. In addition, Chen et al. [72] proposed that water vapor from the western North Pacific Ocean made an important contribution to increasing the precipitation in the QMs. The anomalous anticyclones over the Aleutian Islands and Japan enhanced the easterly water vapor transport in the North Pacific toward the QMs. This allowed the anomalous water vapor in the Arctic Ocean and the North Pacific Ocean to converge, which was conducive to the increase in precipitation in the QMs [73]. Therefore, the change in water vapor from the Pacific Ocean to the QMs in summer remains an open scientific question. In other words, future research should explore whether water vapor from the Pacific Ocean is related to the interannual variation in precipitation in northwest China [71].

Vertical upward movement is the driving factor that forms precipitation. A significant cyclonic circulation anomaly occurred over central Asia on the north side of the South Asian High. This indicated that the westerly circulation at the bottom of the central Asian low trough was stronger, and the summer rainy season was conducive to the enhancement of the convergence and upward movement of the middle and lower troposphere compared with the rainy period [71]. By analyzing the abnormal changes in the average vertical velocity and air temperature at 32.5°N–50°N with longitude and altitude during the rainy period, it was observed that the vertical velocity of 700–200 hPa in northwest China showed a significant negative anomaly. This indicates that the enhancement of upward movement was conducive to the formation of water vapor condensation and precipitation weather [71].

It is well known that the seawater surface temperature directly affects atmospheric circulation, and as a result, the interdecadal and interannual climates undergo change. The study found that around the mid-1980s, the significant decadal shift in the Atlantic

Multidecadal Oscillation (AMO) and Standardized Summer SST over the Indo-Pacific Warm Pool (IPWP) indices was consistent with the interdecadal shift in summer precipitation in the northwest territories [73]. The correlation coefficients of the 11-year average AMO, IPWP correlation coefficient, and precipitation indices were 0.64 and 0.79, respectively, which were significant at the 99% confidence level. This indicates that the decadal variation in summer precipitation in northwest China was closely related to NA (0° – 55° N, 0 – 60° W) and IPWP ocean warming. When both the AMO and IPWP indices are in a positive phase, summer precipitation tends to be abundant in the northwest region [73].

Based on the above analysis, we found that the increase in precipitation in the QMs was closely related to atmospheric circulation and the emissions scenario. Water vapor is the material basis of precipitation, and vertical upward movement is the driving factor of precipitation; the SST also directly affects the atmospheric circulation. Therefore, it is highly important to explore the influence of atmospheric circulation on precipitation in the QMs, which can be studied in the future.

5.2. The Biases and Uncertainty of the Models

Several studies have shown that the applicability of CMIP6 models varies considerably in different regions of the world [74,75]. It is well known that many climate model products have serious shortcomings in terms of precipitation accuracy in high-altitude mountainous areas. These deviations can result from an initial condition bias for atmospheric and oceanic scenarios, physical scenario bias, parametric scheme deviation, and model uncertainty [41,42].

In any model, one source of model uncertainty is convection schemes. The convective scheme has an impact on many aspects of the model simulation, the most important of which is the monsoon simulation. Since the representation of the monsoon state was not explicitly adjusted or tweaked during the model development process, the monsoon simulation was the end product of many other changes and improvements to the multiple parameterizations and formulations in models. Increased moisture sensitivity in deep convection also contributes to model uncertainty. This factor, combined with a warmer SST within the equatorial belt, means that convection is more easily initialized and leads to greater precipitation over land areas involved in the monsoon circulation [76]. In addition, intra-seasonal variability is also enhanced, and these changes in the convective scheme make it easier for the Madden Julian Oscillation (MJO) and the Boreal Summer Intra-seasonal Oscillation (BSISO) events to initialize in the Indian Ocean and propagate eastward and northward, respectively. The QMs are also influenced, to some extent, by the warm and humid air masses of the Indian Ocean during the height of summer. This makes the precipitation in the QMs more variable.

In terms of climate sensitivity, clouds affect the Earth's water budget through precipitation and the Earth's energy budget by regulating solar energy reaching the surface and capturing terrestrial radiation that would otherwise escape to space. This affects the climate, especially precipitation. In the Fifth Assessment Report (AR5) of the Intergovernmental Panel on Climate Change (IPCC), clouds and their feedback were explicitly identified as one of the main remaining challenges in accurately modeling future climate scenarios (IPCC, 2013). Also, internal variability in SST and uncertainty in aerosols in climate models are also sources of bias, which have been found to make it difficult to reproduce decadal variability in the east Asian summer monsoon (EASM) [77].

In terms of a single pattern, taking CESM2 as an example, one of the major sources of bias is climate sensitivity. Gettelman's analysis suggests that the increased climate sensitivity in CESM2 has arisen from a combination of seemingly small changes to cloud microphysics and boundary layer parameters. In addition, this has arisen from land parameter changes that were introduced late in the development process, along with the introduction of more realistic clouds with Cloud Layers Unified By Binormals (CLUBB) [78]. Although the warm tropical SST and improvements in the convective scheme in CESM2 have resulted in an overall improvement in tropical precipitation and a clear impact on

monsoon precipitation in particular, there is still a considerable systematic error in tropical SST. The higher climate sensitivity in CESM2 compared to CESM1 produces greater tropical warming and precipitation increases. Gettelman et al. (2019) [79] showed that cloud feedback in CESM2 has led to an increased equilibrium climate sensitivity, meaning that a doubling of CO₂ has a larger impact on surface temperatures in CESM2. The mean state in CESM2 is cloudier, warmer, and rainier [80]. This was also verified by our evaluation of a single model of CESM2 (see attachment), which showed obvious wet bias in both temporal and spatial distribution (Figures S5–S7). These biases range from being relatively minor, such as local precipitation errors without discernable global affects, to biases that can have significant climate effects such as the moisture deviation in the QMs in CESM2 simulations. The moisture deviation can perhaps be tuned away at the expense of the possible appearance of other biases. There are also much more persistent biases such as the incorrect separation and path of the Gulf Stream–North Atlantic Current system, with accompanying large SST and surface salinity biases. This latter class of biases can have significant climate effects and thus affect precipitation as well, but no robust remedy exists to alleviate them in non-eddy-permitting/non-eddy-resolving ocean models usually used in climate simulations [78].

In this study, MME was chosen to study precipitation in the QMs, which performed relatively well and presented precipitation trends that were almost consistent with the observed data. However, there is still a large uncertainty and room for improvement, as a certain wet bias was presented. In addition to the previous convection scheme of climate sensitivity, this is also related to the simulation of precipitation in mountainous areas and requires higher simulation accuracy. In addition, the existing computational power and applicability of the parameterization scheme make it difficult to meet the simulation requirements. Moreover, each model has its own unique parameterization scheme and model input, so their simulation results can vary greatly.

In addition, there are few observatories in the QMs due to the harsh natural conditions in high-altitude mountains. Most of these observatories are located in the valleys of the QMs. Consequently, there are elevation errors between them and the grid points of the model, which may lead to an underestimation of precipitation. The non-uniform distribution of observatories may also lead to inaccurate model evaluations in areas with few observatories. These deficiencies in the observational data may affect the evaluation of the model in that area [8,81]. So, if the output of the CMIP6 model is corrected, biases may also occur. This is because the precipitation correction of the model is based on the observed data of precipitation. Spatial interpolation methods based on a small number of stations may result in unavoidable errors in alpine regions. Previous studies [82] have depicted that there are differences in precipitation intensity and precipitation frequency from lowland to alpine regions. The interpolation method has been inadequate for precipitation applications in alpine regions. Therefore, improving the precipitation observation accuracy in the QM region is an important basis for future studies of precipitation and extreme precipitation [50].

It is worth mentioning that the horizontal resolution of the CMIP6 global climate model was still relatively low in the study of regional climate change. The ability to simulate the climate in the complex terrain of the QMs remained insufficient [83]. Therefore, in the future, it is necessary to use high-level resolution regional climate models for dynamic downscaling research. Alternatively, an efficient statistical downscaling method could be developed to conduct special prediction studies on the climate of the QMs [84]. To avoid conflating uncertainty in the response of models to a given forcing, it is strongly recommended that models are integrated with the same forcing in the entry card historical simulations and for the forcing uncertainty to be sampled in supplementary simulations [42]. Although this study has analyzed the current variability in precipitation, further research is required to study the relationships between the simulation errors and uncertainties in ensembles of future projections. To explore the causes of uncertainty and systematic errors in individual climate

model simulations, experiments with explicit control of parameter perturbations [85] are required to distinguish the main drivers of uncertainty.

6. Conclusions

Using ERA5 and observations from meteorological stations, this study systematically evaluated the 21 annual global climate models of CMIP6 in the historical period (1959–1988). The temporal and spatial changes in annual precipitation and the precipitation phase (annual snowfall and rainfall) in different future scenarios (SSP126, SSP245, SSP370, and SSP585) were analyzed. The main conclusions are as follows:

- (1) The CMIP6 models exhibited reasonable simulation ability for the spatial distribution of annual precipitation in the QMs. In the historical period, MME was concentrated between 476.99 and 546.96 mm, ERA5 was concentrated between 406.11 and 587.07 mm, and the simulation results were the best in the central region, with an error between -100 and 100 mm. Simulations were low in the north and northeast, and they were high in the south and southeast. The climatic tendency rate of MME was $-2.01 \text{ mm}\cdot 10\text{a}^{-1}$, which was slightly lower than that of ERA5 ($2.82 \text{ mm}\cdot 10\text{a}^{-1}$). It can be seen that MME and ERA5 have a high degree of agreement overall.
- (2) Precipitation and rainfall showed a decreasing trend from southeast to northwest; the more severe the emissions scenario, the more significant the observed decreasing pattern. The trend in snowfall and the snow-to-rain ratio were reversed, showing an increasing trend from southeast to northwest. As the emissions scenario (concentrations of CO_2 , CH_4 , N_2O and other gases) became more severe, the increase became more significant.
- (3) Regarding the time scale, the precipitation in the historical period (1959–1988) fluctuated and rose. From 1959 to 1988, the average seasonal precipitation of MME in spring, summer, autumn, and winter was 130.07, 224.62, 95.96, and 29.07 mm, respectively, and that of ERA5 was 98.57, 280.77, 96.85, and 22.64 mm, respectively. From 2015 to 2100, the difference between the future and historical period from MME, which was especially pronounced in summer, was 21.52, 20.48, 23.00, and 29.24 mm in spring, summer, autumn, and winter, respectively. Meanwhile, the climate tendency rates of average precipitation from MME in spring, summer, autumn, and winter were 5.73, 9.15, 12.23 and $16.14 \text{ mm}\cdot 10\text{a}^{-1}$, respectively. The flood season in the QMs is July and August, and precipitation could reach more than 80 mm. Rainfall rates also rose, while the snowfall and snow-to-rain ratio showed a downward trend; the higher emissions scenario (concentrations of CO_2 , CH_4 , N_2O , and other gases) resulted in a more significant reduction.
- (4) During the period 2015–2100, the snowfall ratio ranged from 0.1 to 1.1. The annual snowfall showed a decreasing trend, the climatic tendency rate ranged from -10 to $0.1 \text{ mm}\cdot 10\text{a}^{-1}$, and the rainfall always showed an increasing trend ($0\text{--}30 \text{ mm}\cdot 10\text{a}^{-1}$), with both passing the significance test ($p < 0.05$). The snow-to-rain ratio was the highest in winter in the four scenarios, with values of 16.77, 17.14, 15.82, and 15.26, because snow is mainly concentrated in winter.

Supplementary Materials: The following supporting information can be downloaded at: <https://www.mdpi.com/article/10.3390/rs15174350/s1>, Table S1. Models that fail the significance test. Figure S1. Spatial distribution of annual seasonal precipitation during the period 2015–2100 from the MME: MAM (a–d), JJA (e–h), SON (i–l), and DJF (m–p). Figure S2. Spatial distribution of differences in annual snowfall over the QMs between four different SSPs (2015–2040, 2041–2070, 2071–2100) and historical period (1959–1988) from MME: SSP126 (a–c), SSP245 (d–f), SSP370 (g–i), and SSP585 (j–l). Figure S3. Spatial distribution of annual rainfall differences over the QMs between four different SSPs (2015–2040, 2041–2070, 2071–2100) and the historical period (1959–1988) from MME: SSP126 (a–c), SSP245 (d–f), SSP370 (g–i), and SSP585 (j–l). Figure S4. Spatial distribution of the annual seasonal S/R ratio trend during the period 2015–2100 from the MME: MAM (a–d), JJA (e–h), SON (i–l), DJF (m–p). Figure S5 Seasonal average precipitation from 1959 to 1988 from CESM2 (a–d) and ERA5

(e–h) for spring (MAM), summer (JJA), autumn (SON) and winter (DJF). Figure S6. Annual cycles of mean monthly precipitation from CESM2 (blue line) and ERA5 (red line) during the period 1959–1988. Figure S7. Time series of annual total precipitation from CESM2 (blue line) and ERA5 (yellow line) during the period 1959–1988 (the shaded part represents one standard deviation).

Author Contributions: Conceptualization, X.Y., W.S., B.H., L.W. and Y.W. (Yuzhe Wang); Writing—original draft preparation, X.Y. and B.H.; Software, J.W., J.C., M.L., Y.W. (Yingshan Wang) and Q.Z. All authors have read and agreed to the published version of the manuscript.

Funding: This research was supported by the National Nature Science Foundation of China (No. 42271145), the Second Tibetan Plateau Scientific Expedition and Research (STEP) program (No. 2019QZKK0106) and the Nature Science Foundation of China (No. 42101120).

Data Availability Statement: Not applicable.

Acknowledgments: We acknowledge the climate modeling groups (listed in Table 1) for producing and sharing their model output. Thanks also to the European Centre for Medium Range Weather Forecasts (ECMWF) for the reanalysis ERA5 data.

Conflicts of Interest: The authors declare no conflict of interest. The funders had no role in the design of the study; in the collection, analyses, or interpretation of data; in the writing of the manuscript; or in the decision to publish the results.

References

- Chen, R.; Han, C.; Wang, L.; Zhao, Y.; Song, Y.; Yang, Y.; Liu, J.; Liu, Z.; Wang, X.; Guo, S.; et al. Surface precipitation and high mountain areas in Qilian Mountains in 2019–2020 Precipitation monitoring significance. *J. Glaciol. Geocryol.* **2023**, *45*, 676–687.
- Yao, T.; Wang, Y.; Liu, S.; Pu, J.; Shen, Y.; Lu, A. Recent glacial retreat in High Asia in China and its impact on water resource in Northwest China. *Sci. China Ser. D Earth Sci.* **2004**, *47*, 1065–1075. [[CrossRef](#)]
- Zhao, C.; Ding, Y.; Yao, S. The variation of precipitation and rain days for different intensity classes during the rainy season in the Qilian Mountains, Northwest China. *Theor. Appl. Climatol.* **2021**, *144*, 163–178. [[CrossRef](#)]
- Yang, B.; Qin, C.; Wang, J.; He, M.; Melvin, T.M.; Osborn, T.J.; Briffa, K.R. A 3500-year tree-ring record of annual precipitation on the northeastern Tibetan Plateau. *Proc. Natl. Acad. Sci. USA* **2014**, *111*, 2903–2908. [[CrossRef](#)]
- Ji, F.; Wu, Z.H.; Huang, J.P.; Chassignet, E.P. Evolution of land surface air temperature trend. *Nat. Clim. Chang.* **2014**, *4*, 462–466. [[CrossRef](#)]
- Han, L.J.; Bai, A.J.; Pu, X.M. Climate change characteristics estimation in the Qilian Mountains based on CMIP6. *Plateau meteorology* **2022**, *41*, 864–875.
- Qin, D.; Zhen, C.; Yong, L.; Yihui, D.; Dai, X.S.; Jia, W.R. The latest understanding of climate change science. *Prog. Clim. Chang. Res.* **2007**, *3*, 63–73.
- Li, Y.Z.; Qin, X.; Liu, Y.S.; Jin, Z.Z.; Liu, J.; Wang, L.H.; Chen, J.Z. Evaluation of Long-Term and High-Resolution Gridded Precipitation and Temperature Products in the Qilian Mountains, Qinghai-Tibet Plateau. *Front. Environ. Sci.* **2022**, *10*, 906821. [[CrossRef](#)]
- Shi, Y.; Shen, Y. A preliminary study on the signals, impacts and prospects of the transition of climate from warm dry to warm and humid climate in northwest China. *Sci. Technol. Rev.* **2003**, *23*, 54–57. [[CrossRef](#)]
- Li, D.L.; Xie, J.N.; Wang, W. Study on summer precipitation characteristics and anomalies in northwest China. *Atmos. Sci.* **1997**, *21*, 76–85. [[CrossRef](#)]
- Ma, Z.G. The evolution of dry and wet in northern China and its possible connection with regional warming. *Chin. J. Geophys.* **2005**, *48*, 1011–1018. [[CrossRef](#)]
- Qin, D.H.; Yao, T.D.; Ding, Y.J.; Ren, J.W. The establishment of the cryosphere scientific system and its significance. *Bull. Chin. Acad. Sci.* **2020**, *35*, 394–406. [[CrossRef](#)]
- Wang, L.; Ren, S.C.; Yao, X.S. Research review on calculation methods and influential factors on areal precipitation of alpine mountains. *Plateau Meteorol.* **2017**, *36*, 1546–1556.
- Zhao, T.; Fu, C.; Ke, Z.; Guo, W. Global Atmosphere Reanalysis Datasets: Current Status and Recent Advances. *Adv. Earth Sci.* **2010**, *25*, 241.
- Chen, L.; Frauenfeld, O.W. A comprehensive evaluation of precipitation simulations over China based on CMIP5 multimodel ensemble projections. *J. Geophys. Res. Atmos.* **2014**, *119*, 5767–5786. [[CrossRef](#)]
- Fan, X.W.; Duan, Q.Y.; Shen, C.W.; Wu, Y.; Xing, C. Global surface air temperatures in CMIP6: Historical performance and future changes. *Environ. Res. Lett.* **2020**, *15*, 14. [[CrossRef](#)]
- Wei, C.; Da, B.J.; Xiao, X.W. Evaluation and Projection of CMIP6 Models for Climate over the Qinghai-Xizang (Tibetan) Plateau. *Plateau Meteorol.* **2021**, *40*, 1455–1469.
- Qin, H.; Da, B.J.; Guang, Z.F. Evaluation of CMIP5 models over the Qinghai-Tibetan Plateau. *Chin. J. Atmos. Sci.* **2014**, *38*, 924–938.

19. Zhen, C.L.; Zhi, G.W.; Shi, H.L.; Yan, H.G.; Bo, H.; Suo, L. Verifications of surface air temperature and precipitation from CMIP5 Model in Northern Hemisphere and Qinghai Xizang Plateau. *Plateau Meteorol.* **2013**, *32*, 921–928.
20. Jing, W.; Bao, J.W.; Yan, F.Y.; Yan, C.; Lin, C.; Jian, C.Y.; Xin, W.L. Comparing simulated temperature and precipitation of CMIP3 and CMIP5 in arid areas of Northwest China. *Clim. Chang. Res.* **2017**, *13*, 198–212.
21. Stocker, T. *Climate Change 2013: The Physical Science Basis: Working Group I Contribution to the Fifth Assessment Report of the Intergovernmental Panel on Climate Change*; Cambridge University Press: Cambridge, UK, 2014.
22. Ying, X.; Chong, H.X. Preliminary assessment of simulations of climate changes over China by CMIP5 multi-models. *Atmos. Ocean. Sci. Lett.* **2012**, *5*, 489–494. [[CrossRef](#)]
23. Su, F.; Duan, X.; Chen, D.; Hao, Z.; Cuo, L. Evaluation of the Global Climate Models in the CMIP5 over the Tibetan Plateau. *J. Clim.* **2013**, *26*, 3187–3208. [[CrossRef](#)]
24. Moss, R.H.; Edmonds, J.A.; Hibbard, K.A.; Manning, M.R.; Rose, S.K.; van Vuuren, D.P.; Carter, T.R.; Emori, S.; Kainuma, M.; Kram, T.; et al. The next generation of scenarios for climate change research and assessment. *Nature* **2010**, *463*, 747–756. [[CrossRef](#)] [[PubMed](#)]
25. Tian, J.Z.; Wen, X.Z.; Xiao, L.C.; Li, X.Z.; Li, W.Z.; Wen, M.M. The nearterm, mid-term and long-term projections of temperature and precipitation changes over the Tibetan Plateau and the sources of uncertainties. *J. Meteorol. Sci.* **2020**, *40*, 697–710.
26. Zhou, T.J.; Zou, L.W.; Chen, X.L. Review of the Sixth International Coupling Model Comparison Program (CMIP6). *Prog. Clim. Chang. Res.* **2019**, *15*, 445–456.
27. Gusain, A.; Ghosh, S.; Karmakar, S. Added value of CMIP6 over CMIP5 models in simulating Indian summer monsoon rainfall. *Atmos. Res.* **2020**, *232*, 8. [[CrossRef](#)]
28. Rivera, J.A.; Arnould, G. Evaluation of the ability of CMIP6 models to simulate precipitation over Southwestern South America: Climatic features and long-term trends (1901–2014). *Atmos. Res.* **2020**, *241*, 15. [[CrossRef](#)]
29. O'Neill, B.C.; Tebaldi, C.; van Vuuren, D.P.; Eyring, V.; Friedlingstein, P.; Hurtt, G.; Knutti, R.; Kriegler, E.; Lamarque, J.F.; Lowe, J.; et al. The Scenario Model Intercomparison Project (ScenarioMIP) for CMIP6. *Geosci. Model Dev.* **2016**, *9*, 3461–3482. [[CrossRef](#)]
30. Ullah, I.; Saleem, F.; Iyakaremye, V.; Yin, J.; Ma, X.; Syed, S.; Hina, S.; Asfaw, T.G.; Omer, A. Projected Changes in Socioeconomic Exposure to Heatwaves in South Asia under Changing Climate. *Earth's Future* **2022**, *10*, e2021EF002240. [[CrossRef](#)]
31. Wu, J.; Shi, Y.; Xu, Y. Evaluation and Projection of Surface Wind Speed Over China Based on CMIP6 GCMs. *J. Geophys. Res. Atmos.* **2020**, *125*, e2020JD033611. [[CrossRef](#)]
32. Zhao, S.; Yu, Y.; Lin, P.; Liu, H.; He, B.; Bao, Q.; Guo, Y.; Hua, L.; Chen, K.; Wang, X. Datasets for the CMIP6 Scenario Model Intercomparison Project (ScenarioMIP) Simulations with the Coupled Model CAS FGOALS-f3-L. *Adv. Atmos. Sci.* **2021**, *38*, 329–339. [[CrossRef](#)]
33. Chen, R.S.; Han, C.T.; Liu, J.F.; Yang, Y.; Liu, Z.W.; Wang, L.; Kang, E.S. Maximum precipitation altitude on the northern flank of the Qilian Mountains, northwest China. *Hydrol. Res.* **2018**, *49*, 1696–1710. [[CrossRef](#)]
34. Lv, Y.M.; Li, Z.S.; Feng, Q.; Li, Y.G.; Yuan, R.F.; Gui, J.; Li, Z.J.; Zhang, B.J. Research on extreme temperature changes in Qilian Mountains in the past 60 years. *Plateau Meteorol.* **2019**, *38*, 959–970.
35. Yin, X.; Zhang, Q.; Xu, Q.; Xue, W.; Guo, H.; Shi, Z. Research on the characteristics of climate change in the Qilian Mountains in the past 50 years. *Plateau Meteorol.* **2009**, *28*, 85–90.
36. LI, Y. Tree-Ring Based Climate Reconstruction for Qilian Mountain. Master's Thesis, Lanzhou University, Lanzhou, China, 2011.
37. Yao, Z. Climatic Variation over Qilian Mountain Region in last 50 Years. Master's Thesis, Northwest Normal University, Lanzhou, China, 2009.
38. Li, Z.X.; Yuan, R.F.; Feng, Q.; Zhang, B.J.; Lv, Y.M.; Li, Y.G.; Wei, W.; Chen, W.; Ning, T.T.; Gui, J.; et al. Climate background, relative rate, and runoff effect of multiphase water transformation in Qilian Mountains, the third pole region. *Sci. Total Environ.* **2019**, *663*, 315–328. [[CrossRef](#)] [[PubMed](#)]
39. Liu, S.; Yao, X.; Guo, W.Q.; Xu, J.; Shangguan, D.; Wei, J.; Bao, W.; Wu, L. The contemporary glaciers in China based on the second Chinese glacier inventory. *Acta Geogr. Sin.* **2015**, *70*, 3–16. [[CrossRef](#)]
40. Chen, Z.K. Study on Characteristics of the Precipitation in Qilian Mountain during Recent 40 Years. Master's Thesis, Lanzhou University, Lanzhou, China, 2012.
41. Zhang, L.X.; Chen, X.L.; Xin, X.G. Overview and review of the CMIP6 ScenarioMIP. *Prog. Clim. Chang. Res.* **2019**, *15*, 519–525.
42. Eyring, V.; Bony, S.; Meehl, G.A.; Senior, C.A.; Stevens, B.; Stouffer, R.J.; Taylor, K.E. Overview of the Coupled Model Intercomparison Project Phase 6 (CMIP6) experimental design and organization. *Geosci. Model Dev.* **2016**, *9*, 1937–1958. [[CrossRef](#)]
43. Colette, A.; Ancellet, G. Impact of vertical transport processes on the tropospheric ozone layering above Europe. Part II: Climatological analysis of the past 30 years. *Atmos. Environ.* **2005**, *39*, 5423–5435. [[CrossRef](#)]
44. Herman, J.R. Global increase in UV irradiance during the past 30 years (1979–2008) estimated from satellite data. *J. Geophys. Res.-Atmos.* **2010**, *115*, 15. [[CrossRef](#)]
45. Velden, C.; Harper, B.; Wells, F.; Beven, J.L.; Ehr, R.; Olander, T.; Mayfield, M.; Guard, C.C.; Lander, M.; Edson, R.; et al. The Dvorak tropical cyclone intensity estimation technique. *Bull. Am. Meteorol. Soc.* **2006**, *87*, 1195–1210. [[CrossRef](#)]
46. Li, C.; Zhao, T.; Shi, C.; Liu, Z. Evaluation of Daily Precipitation Product in China from the CMA Global Atmospheric Interim Reanalysis. *J. Meteorol. Res.* **2020**, *34*, 117–136. [[CrossRef](#)]
47. Wang, A.; Lettenmaier, D.P.; Sheffield, J. Soil Moisture Drought in China, 1950–2006. *J. Clim.* **2011**, *24*, 3257–3271. [[CrossRef](#)]

48. Arshad, M.; Ma, X.; Yin, J.; Ullah, W.; Liu, M.; Ullah, I. Performance evaluation of ERA-5, JRA-55, MERRA-2, and CFS-2 reanalysis datasets, over diverse climate regions of Pakistan. *Weather Clim. Extrem.* **2021**, *33*, 100373. [[CrossRef](#)]
49. Zhu, Y.Y.; Yang, S.N. Evaluation of CMIP6 for historical temperature and precipitation over the Tibetan Plateau and its comparison with CMIP5. *Adv. Clim. Chang. Res.* **2020**, *11*, 239–251. [[CrossRef](#)]
50. Li, Y.; Qin, X.; Jin, Z.; Liu, Y. Future Projection of Extreme Precipitation Indices over the Qilian Mountains under Global Warming. *Int. J. Environ. Res. Public Health* **2023**, *20*, 4961. [[CrossRef](#)] [[PubMed](#)]
51. Qiang, F.; Zhang, M.J.; Wang, S.J.; Liu, Y.M.; Ren, Z.G.; Zhu, X.F. Estimation of areal precipitation in the Qilian Mountains based on a gridded dataset since 1961. *J. Geogr. Sci.* **2016**, *26*, 59–69. [[CrossRef](#)]
52. Li, Z.X.; Qi, F.; Song, Y.; Wang, Q.J.; Yang, J.; Li, Y.G.; Li, J.G.; Guo, X.Y. Stable isotope composition of precipitation in the south and north slopes of Wushaoling Mountain, northwestern China. *Atmos. Res.* **2016**, *182*, 87–101. [[CrossRef](#)]
53. Gong, N.; Sun, M.; Yan, L.; Gong, P.; Ma, X.; Mou, J. Temporal and spatial characteristics of atmospheric water vapor and its relationship with precipitation in Qilian Mountains during 1979–2016. *Arid Land Geogr.* **2017**, *40*, 762–771.
54. Chen, S.Y.; Dong, A.X.; Han, T. Differences in Summer Precipitation between the East and West of the Qilian Mountains and Its Contributing Factors. *J. Nanjing Inst. Meteorol.* **2007**, *30*, 715–719.
55. Gao, Z.G. Simulation study on the influence of mesoscale topography in East China on heavy rainfall in northern Zhejiang. *Acta Geogr. Sin.* **1994**, *52*.
56. Lin, Q.G.; Wang, L.B.; Zhang, J.H. Assessment of the risk and population exposure of rainfall-induced geological disasters in China under the scenarios of global temperature rise of 1.5 °C and 2.0 °C. *J. Geo. Inf. Sci.* **2023**, *25*, 177–189.
57. Johns, T.C.; Royer, J.F.; Hoschel, I.; Huebener, H.; Roeckner, E.; Manzini, E.; May, W.; Dufresne, J.L.; Ottera, O.H.; van Vuuren, D.P.; et al. Climate change under aggressive mitigation: The ENSEMBLES multi-model experiment. *Clim. Dyn.* **2011**, *37*, 1975–2003. [[CrossRef](#)]
58. Zhu, X.W.; Sun, Y.C.; Tan, Z.Q.; Liu, J.J. Variation characteristics of the Somali trans-equatorial flow and its impact on summer precipitation in the eastern Northwest Territories. *Desert Oasis Weather* **2019**, *13*, 7–12.
59. Du, W.; Kang, S.; Qian, L.; Jiang, Y.; Sun, W.; Chen, J.; Xu, Z.; Sun, W.; Qin, X.; Chai, X. Spatiotemporal Variation of Snow Cover Frequency in the Qilian Mountains (Northwestern China) during 2000–2020 and Associated Circulation Mechanisms. *Remote Sens.* **2022**, *14*, 2823.
60. Deng, H.; Pepin, N.C.; Chen, Y. Changes of snowfall under warming in the Tibetan Plateau. *J. Geophys. Res. Atmos.* **2017**, *122*, 7323–7341. [[CrossRef](#)]
61. Liu, S.Y. Glacier retreat as a result of climate warming and increased precipitation in the Tarim river basin, northwest China. *Ann. Glaciol.* **2017**, *43*, 91–96. [[CrossRef](#)]
62. Fujita, K. Influence of precipitation seasonality on glacier mass balance and its sensitivity to climate change. *Ann. Glaciol.* **2017**, *48*, 88–92. [[CrossRef](#)]
63. Frauenfeld, O.W.; Zhang, T.J.; Serreze, M.C. Climate change and variability using European Centre for Medium-Range Weather Forecasts reanalysis (ERA-40) temperatures on the Tibetan Plateau. *J. Geophys. Res. Atmos.* **2005**, *110*, D2. [[CrossRef](#)]
64. Ma, L.J.; Zhang, T.J.; Li, Q.X.; Frauenfeld, O.W.; Qin, D. Evaluation of ERA-40, NCEP-1, and NCEP-2 reanalysis air temperatures with ground-based measurements in China. *J. Geophys. Res. Atmos.* **2008**, *113*, D15. [[CrossRef](#)]
65. Mao, J.F.; Shi, X.Y.; Ma, L.J.; Kaiser, D.P.; Li, Q.X.; Thornton, P.E. Assessment of Reanalysis Daily Extreme Temperatures with China's Homogenized Historical Dataset during 1979–2001 Using Probability Density Functions. *J. Clim.* **2010**, *23*, 6605–6623. [[CrossRef](#)]
66. Yang, K.; Guo, X.F.; He, J.; Qin, J.; Koike, T. On the Climatology and Trend of the Atmospheric Heat Source over the Tibetan Plateau: An Experiments-Supported Revisit. *J. Clim.* **2011**, *24*, 1525–1541. [[CrossRef](#)]
67. Ullah, I.; Ma, X.Y.; Yin, J.; Omer, A.; Habtemicheal, B.A.; Saleem, F.; Iyakaremye, V.; Syed, S.; Arshad, M.; Liu, M.Y. Spatiotemporal characteristics of meteorological drought variability and trends (1981–2020) over South Asia and the associated large-scale circulation patterns. *Clim. Dyn.* **2022**, *60*, 2261–2284. [[CrossRef](#)]
68. Lu, S.; Hu, Z.; Yu, H.; Fan, W.; Fu, C.; Wu, D. Changes of Extreme Precipitation and its Associated Mechanisms in Northwest China. *Adv. Atmos. Sci.* **2021**, *38*, 1665–1681. [[CrossRef](#)]
69. Xin, G.D.; Kai, J.Z. Analysis of the decadal variation mechanism of precipitation in northwest and western China in the second 30 years of the 20th century. *Acta Phys. Sin.* **2012**, *61*, 199201. [[CrossRef](#)]
70. Kang, X.; Jinhai, H.; Congwen, Z. The interdecadal linkage of the summer precipitation in eastern China with the surface air temperature over Lake Baikal in the past 50 years. *J. Meteorol.* **2011**, *69*, 570–580.
71. Xue, T.; Ding, Y.H.; Lu, C.H. Interdecadal Variability of Summer Precipitation in Northwest China and Associated Atmospheric Circulation Changes. *J. Meteorol. Res.* **2022**, *36*, 824–840. [[CrossRef](#)]
72. Chen, C.; Zhang, X.; Lu, H.; Jin, L.; Du, Y.; Chen, F. Increasing summer precipitation in arid Central Asia linked to the weakening of the East Asian summer monsoon in the recent decades. *Int. J. Climatol.* **2021**, *41*, 1024–1038. [[CrossRef](#)]
73. Wu, P.; Liu, Y.J.; Ding, Y.H.; Li, X.C.; Wang, J. Modulation of sea surface temperature over the North Atlantic and Indian-Pacific warm pool on interdecadal change of summer precipitation over northwest China. *Int. J. Climatol.* **2022**, *42*, 8526–8538. [[CrossRef](#)]
74. Dong, T.; Dong, W. Evaluation of extreme precipitation over Asia in CMIP6 models. *Clim. Dyn.* **2021**, *57*, 1751–1769. [[CrossRef](#)]
75. Akisanola, A.A.; Ongoma, V.; Kooperman, G.J. Evaluation of CMIP6 models in simulating the statistics of extreme precipitation over Eastern Africa. *Atmos. Res.* **2021**, *254*, 105509. [[CrossRef](#)]

76. Meehl, G.A.; Shields, C.; Arblaster, J.M.; Annamalai, H.; Neale, R. Intraseasonal, Seasonal, and Interannual Characteristics of Regional Monsoon Simulations in CESM2. *J. Adv. Model. Earth Syst.* **2020**, *12*, e2019MS001962. [[CrossRef](#)]
77. Xin, X.G.; Wu, T.W.; Zhang, J.; Yao, J.C.; Fang, Y.J. Comparison of CMIP6 and CMIP5 simulations of precipitation in China and the East Asian summer monsoon. *Int. J. Climatol.* **2020**, *40*, 6423–6440. [[CrossRef](#)]
78. Danabasoglu, G.; Lamarque, J.F.; Bacmeister, J.; Bailey, D.A.; DuVivier, A.K.; Edwards, J.; Emmons, L.K.; Fasullo, J.; Garcia, R.; Gettelman, A.; et al. The Community Earth System Model Version 2 (CESM2). *J. Adv. Model. Earth Syst.* **2020**, *12*, e2019MS001916. [[CrossRef](#)]
79. Gettelman, A.; Hannay, C.; Bacmeister, J.T.; Neale, R.B.; Pendergrass, A.G.; Danabasoglu, G.; Lamarque, J.-F.; Fasullo, J.T.; Bailey, D.A.; Lawrence, D.M.; et al. High Climate Sensitivity in the Community Earth System Model Version 2 (CESM2). *Geophys. Res. Lett.* **2019**, *46*, 8329–8337. [[CrossRef](#)]
80. McIlhatten, E.A.; Kay, J.E.; L'Ecuyer, T.S. Arctic Clouds and Precipitation in the Community Earth System Model Version 2. *J. Geophys. Res. Atmos.* **2020**, *125*, e2020JD032521. [[CrossRef](#)]
81. Huai, B.; Wang, J.; Sun, W.; Wang, Y.; Zhang, W. Evaluation of the near-surface climate of the recent global atmospheric reanalysis for Qilian Mountains, Qinghai-Tibet Plateau. *Atmos. Res.* **2021**, *250*, 105401. [[CrossRef](#)]
82. Ding, Y.J. Precipitation conditions for the development of the present glaciers on the Northern Slope of Karakorum. *GeoJournal* **1991**, *25*, 243–248. [[CrossRef](#)]
83. Zhang, X.; Hua, L.; Jiang, D. Assessment of CMIP6 model performance for temperature and precipitation in Xinjiang, China. *Atmos. Ocean. Sci. Lett.* **2022**, *15*, 100128. [[CrossRef](#)]
84. Xiao, Z.; Xiao, W.; Li, H. CMIP6 model estimation of temperature and precipitation changes in Xinjiang. *Chin. J. Atmos. Sci.* **2023**, *47*, 387–398. [[CrossRef](#)]
85. Rougier, J.; Sexton, D.M.H.; Murphy, J.M.; Stainforth, D. Analyzing the Climate Sensitivity of the HadSM3 Climate Model Using Ensembles from Different but Related Experiments. *J. Clim.* **2009**, *22*, 3540–3557. [[CrossRef](#)]

Disclaimer/Publisher's Note: The statements, opinions and data contained in all publications are solely those of the individual author(s) and contributor(s) and not of MDPI and/or the editor(s). MDPI and/or the editor(s) disclaim responsibility for any injury to people or property resulting from any ideas, methods, instructions or products referred to in the content.